



Disequilibrium Chemistry, Diabatic Thermal Structure, and Clouds in the Atmosphere of COCONUTS-2b

Zhoujian Zhang (张周健)^{1,9}, Sagnick Mukherjee¹, Michael C. Liu², Jonathan J. Fortney¹, Emily Mader¹, William M. J. Best³, Trent J. Dupuy⁴, Sandy K. Leggett⁵, Theodora Karalidi⁶, Michael R. Line⁷, Mark S. Marley⁸, Caroline V. Morley³, Mark W. Phillips⁴, Robert J. Siverd², and Joseph A. Zalesky⁷

¹ Department of Astronomy & Astrophysics, University of California, Santa Cruz, CA 95064, USA

² Institute for Astronomy, University of Hawai'i at Mānoa, 2680 Woodlawn Drive, Honolulu, HI 96822, USA

³ The University of Texas at Austin, Department of Astronomy, 2515 Speedway, C1400, Austin, TX 78712, USA

⁴ Institute for Astronomy, University of Edinburgh, Royal Observatory, Blackford Hill, Edinburgh, EH9 3HJ, UK

⁵ Gemini Observatory/NFS's NOIRLab, 670 North A'ohoku Place, Hilo, HI 96720, USA

⁶ Department of Physics, University of Central Florida, 4111 Libra Drive, Orlando, FL 32816, USA

⁷ School of Earth and Space Exploration, Arizona State University, Tempe, AZ 85281, USA

⁸ Lunar & Planetary Laboratory, University of Arizona, Tucson, AZ 85721, USA

Received 2024 August 1; revised 2024 October 5; accepted 2024 October 17; published 2024 December 6

Abstract

Located 10.888 pc from Earth, COCONUTS-2b is a planetary-mass companion to a young (150–800 Myr) M3 star, with a wide orbital separation (6471 au) and a low companion-to-host mass ratio (0.021 ± 0.005). We have studied the atmospheric properties of COCONUTS-2b using newly acquired 1.0–2.5 μm spectroscopy from Gemini/Flamingos-2. The spectral type of COCONUTS-2b is refined to $T_{\text{eff}} = 795 \pm 50$ K based on comparisons with T/Y dwarf spectral templates. We have conducted an extensive forward-modeling analysis, comparing the near-infrared spectrum and mid-infrared broadband photometry of COCONUTS-2b with 16 state-of-the-art atmospheric model grids developed for brown dwarfs and self-luminous exoplanets near the T/Y transition. The PH₃-free ATMO2020++, ATMO2020++, and EXO-REM models best match the specific observations of COCONUTS-2b, regardless of variations in the input spectrophotometry. This analysis suggests the presence of disequilibrium chemistry, along with a diabatic thermal structure and/or clouds, in the atmosphere of COCONUTS-2b. All models predict fainter Y-band fluxes than observed, highlighting uncertainties in the alkali chemistry models and opacities. We determine a bolometric luminosity of $\log(L_{\text{bol}}/L_{\odot}) = -6.18$ dex, with a 0.5 dex wide range of $[-6.43, -5.93]$ dex that accounts for various assumptions of atmospheric models. Using several thermal evolution models, we derive an effective temperature of $T_{\text{eff}} = 483^{+44}_{-53}$ K, a surface gravity of $\log(g) = 4.19^{+0.18}_{-0.13}$ dex, a radius of $R = 1.11^{+0.03}_{-0.04} R_{\text{Jup}}$, and a mass of $M = 8 \pm 2 M_{\text{Jup}}$. Various atmospheric model grids consistently indicate that COCONUTS-2b's atmosphere likely has subsolar or near-solar metallicity and C/O. These findings provide valuable insights into COCONUTS-2b's formation history and the potential outward migration to its current wide orbit.

Unified Astronomy Thesaurus concepts: Exoplanet atmospheres (487); T dwarfs (1679); Y dwarfs (1827)

1. Introduction

There has been a remarkable surge in spectroscopic observations of exoplanets over the past few years, powered by new-generation ground-based facilities and the James Webb Space Telescope (JWST; e.g., GRAVITY Collaboration et al. 2020; P. Mollière et al. 2020; J. J. Wang et al. 2021; Y. Zhang et al. 2021; L. Alderson et al. 2023; P. C. August et al. 2023; J. L. Bean et al. 2023; S. A. Beiler et al. 2023; L.-P. Coulombe et al. 2023; A. D. Feinstein et al. 2023; J. Lustig-Yaeger et al. 2023; JWST Transiting Exoplanet Community Early Release Science Team et al. 2023; B. E. Miles et al. 2023; N. Madhusudhan et al. 2023; S. E. Moran et al. 2023; S.-M. Tsai et al. 2023; Z. Rustamkulov et al. 2023; S. Zieba et al. 2023; S. A. Beiler et al. 2024; M. Hammond et al. 2024; H. Kothari et al. 2024; S. Petrus et al. 2024). These spectra offer quantitative insights into the atmospheres, formation, and evolution of the

diverse population of exoplanets, uncovering rich information about the physical and chemical processes in their atmospheres (for recent reviews, see M. S. Marley & T. D. Robinson 2015; J. J. Fortney 2018; X. Zhang 2020; R. Wordsworth & L. Kreidberg 2022; T. Currie et al. 2023; E. M.-R. Kempton & H. A. Knutson 2024). These processes include vertical mixing, horizontal transport, cloud condensation, formation of photochemical hazes, hot spots, mass loss, planetesimal accretion, and auroral emission (e.g., J. J. Fortney 2005; A. P. Showman et al. 2009; D. K. Sing et al. 2016; D. Apai et al. 2017; M. Mansfield et al. 2018; P. Mollière et al. 2020; P. Gao et al. 2021; M. Mansfield et al. 2021; Y. Zhang et al. 2021a; S. Mukherjee et al. 2022; K. K. W. Hoch et al. 2023; A. Madurowicz et al. 2023; Z. Zhang et al. 2023a, 2023b; M. Gully-Santiago et al. 2024; J. K. Faherty et al. 2024; J. Inglis et al. 2024; J. W. Xuan et al. 2024a). Moreover, the atmospheric compositions of exoplanets and brown dwarfs, as measured from spectra, exhibit trends that can be contextualized with those observed in our solar system, providing crucial insights into their formation pathways (e.g., L. Welbanks et al. 2019; Y. Zhang et al. 2021; D. Barrado et al. 2023; K. K. W. Hoch et al. 2023; Z. Zhang et al. 2023a; B. W. P. Lew et al. 2024; E. Nasedkin et al. 2024; J. W. Xuan et al. 2024b).

⁹ NASA Sagan Fellow.

Original content from this work may be used under the terms of the Creative Commons Attribution 4.0 licence. Any further distribution of this work must maintain attribution to the author(s) and the title of the work, journal citation and DOI.

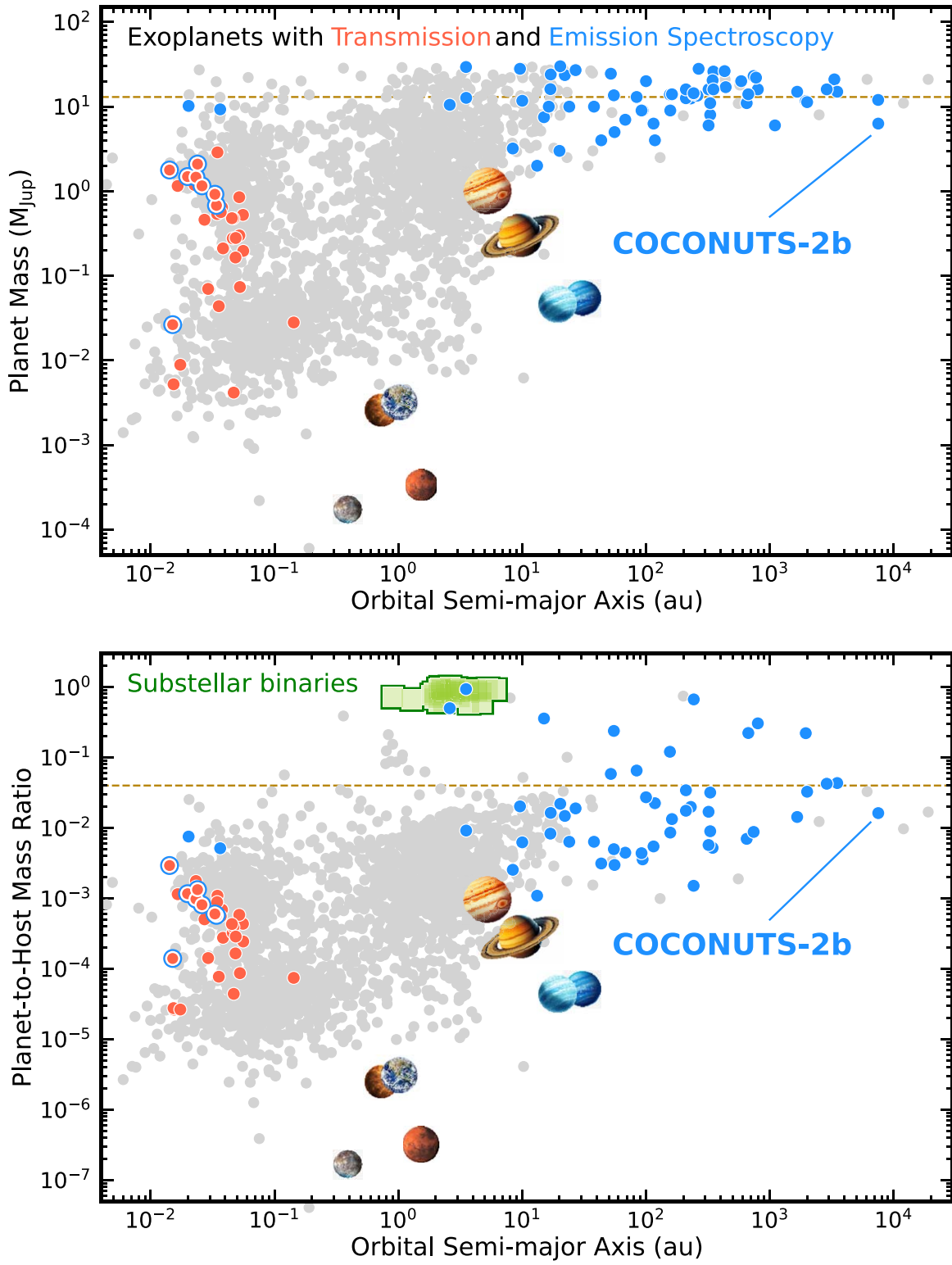


Figure 1. Masses (top) or mass ratios (bottom) of confirmed exoplanets (collected from the NASA Exoplanet Archive on 2024 June 21) as functions of their orbital separations (gray), with those having observed transmission and emission spectra highlighted in orange and blue, respectively. Substellar binaries with dynamical masses are shown in green (T. J. Dupuy et al. 2016; T. J. Dupuy & M. C. Liu 2017; P. F. Lazorenko & J. Sahlmann 2018; T. J. Dupuy et al. 2019; G. Chabrier et al. 2023; T. J. Dupuy et al. 2023). Solar system planets are plotted with sizes unscaled. Brown-dashed lines highlight the planet mass of $13 M_{Jup}$ and the planet-to-host mass ratio of 0.04, as adopted by the IAU working definition of exoplanets.

However, only a relatively small portion of known exoplanets have had their transmission or emission spectra observed so far (Figure 1). Among the 5548 confirmed exoplanets as of 2024 June 21 (NASA Exoplanet Science

Institute 2024), transmission spectra have been obtained for 44 objects, emission spectra for 69 objects, and both types of spectra for 10 objects, with each spectrum containing more than 10 data points. Observing transmission spectra is

challenging due to the planets' relatively small transit depths, the activity and starspots of some planet-host stars, and the potential absence of detectable exoplanetary atmospheres. For emission spectroscopy, most data have been collected for directly imaged, self-luminous planets that reside on relatively wide orbits ($\gtrsim 10$ au) with high masses ($\gtrsim 2 M_{\text{Jup}}$; for reviews, see W. A. Traub & B. R. Oppenheimer 2010; B. P. Bowler 2016; T. Currie et al. 2023). The primary challenge of such observations arises from the contaminating light of these planets' much brighter host stars (over 10^4 times brighter in flux) at small angular separations ($< 1''$).

COCONUTS-2b (WISEPA J075108.79–763449.6; Z. Zhang et al. 2021a) is a remarkable self-luminous planetary-mass object suitable for high-quality spectroscopy. This object's thermal emission can be distinctly detected from that of its parent star due to the wide projected separation (6471 au or $594''$; Figure 1). COCONUTS-2b was initially considered a free-floating T9 brown dwarf, as found by J. D. Kirkpatrick et al. (2011). Z. Zhang et al. (2021a) established its physical association with a well-known young M3 star, COCONUTS-2A (L 34–26), based on their consistent parallaxes and proper motions. Z. Zhang et al. (2021a) assigned an age of 150–800 Myr to the COCONUTS-2A+b system, using indicators such as the host star's alkali lines, absence of lithium absorption, strong H α emission, UV and X-ray luminosities, rotation, kinematics, and position in the HR diagram (see their Section 3.2). According to the BANYAN Σ tool¹⁰ developed by J. Gagné et al. (2018), COCONUTS-2A is not associated with any known young moving groups. However, an updated version of BANYAN Σ suggests that COCONUTS-2A may be a candidate member of the ~ 400 Myr-old Ursa Major association (F. Marocco et al. 2024), as proposed by J. Gagné et al. (2020). This potential membership supports the age estimates of 150–800 Myr established by Z. Zhang et al. (2021a). Furthermore, by combining the stellar radius, rotation period and the projected rotation velocity, Z. Zhang et al. (2021a) suggested that the spin axis of COCONUTS-2A has a nearly edge-on inclination. B. P. Bowler et al. (2023) quantified this stellar inclination to $80^\circ 2^{+9}_{-4}{}^{\circ}$, with the probability distribution peaking at 90° .

With a planetary mass ($8 \pm 2 M_{\text{Jup}}$) and a low mass ratio relative to its parent star (0.021 ± 0.005),¹¹ COCONUTS-2b satisfies the IAU working definition of an exoplanet¹² at the time of writing (Figure 1). However, the formation pathway of COCONUTS-2b remains elusive, especially given the wide orbital separation from its parent star (see discussions in Z. Zhang et al. 2021a; F. Marocco et al. 2024). One possibility is that COCONUTS-2b formed within the circumstellar disk of COCONUTS-2A and subsequently migrated outward through dynamical interactions (e.g., E. I. Vorobyov 2013). Alternatively, COCONUTS-2b may have formed via gravitational instability in a collapsing molecular cloud, similar to the secondary components in stellar-binary systems, given that its mass is close to the estimated lower mass limit for star formation products (e.g., B. Zuckerman & I. Song 2009; J. D. Kirkpatrick et al. 2021). Additionally, F. Marocco et al. (2024) discussed that COCONUTS-2b might be a captured

object from a flyby; they suggested that while this scenario is possible, it is less likely due to the high relative velocities typically expected between the two objects.

COCONUTS-2b has extreme properties. Located at 10.888 ± 0.002 pc¹³ (C. A. L. Bailer-Jones et al. 2021), it is the second-nearest directly imaged planet to the solar system (after Eps Ind Ab; E. C. Matthews et al. 2024). COCONUTS-2b has the second-coldest effective temperature (after WD0806-661 B; K. L. Luhman et al. 2011) and the second-widest orbit (after TYC 9486-927-1 b; N. R. Deacon et al. 2016) among all imaged exoplanets to date. Additionally, the bolometric luminosity and age of COCONUTS-2b are consistent with both hot-start and cold-start thermal evolution models, a characteristic shared by only three other objects among all the known directly imaged exoplanets and brown dwarfs: WD 0806-661 B (K. L. Luhman et al. 2011), 51 Eri b (B. Macintosh et al. 2015), and AF Lep b (K. Franson et al. 2023; D. Mesa et al. 2023; R. J. De Rosa et al. 2023). Among these four objects, the post-formation entropies and/or formation epochs of 51 Eri b and AF Lep b can be constrained by warm-start thermal evolution models based on these objects' directly measured luminosities and dynamical masses (T. J. Dupuy et al. 2022; Z. Zhang 2024a). However, this analysis cannot be applied to COCONUTS-2b as yet, due to the difficulties in measuring its dynamical mass given its slow orbital motion at such a wide separation from its parent star.

The atmospheric properties of COCONUTS-2b have been studied through its photometry in the literature. Comparing the [3.6]–[4.5] and J–[4.5] colors with the atmospheric models of P. Tremblin et al. (2015), S. K. Leggett et al. (2017) suggested that this object is likely a subdwarf with a low metallicity. J. D. Kirkpatrick et al. (2021) found that the absolute magnitudes of COCONUTS-2b in the H , $W1$, and [3.6] bands are fainter than those of brown dwarfs with similar [3.6]–[4.5] colors. Additionally, Z. Zhang et al. (2021a) compared the observed broadband photometry with several atmospheric models, finding evidence of both disequilibrium chemistry and clouds in the atmosphere of COCONUTS-2b.

We present new near-infrared spectra of COCONUTS-2b collected from the Gemini-South telescope (Section 2). Comparing these data with T and Y brown dwarf spectral templates results in a slightly updated spectral type of $T9.5 \pm 0.5$ (Section 3). To estimate the atmospheric properties of COCONUTS-2b, we compare its Gemini spectrum with 16 state-of-the-art atmospheric model grids of T/Y dwarfs (Section 4). These atmospheric model grids have various assumptions, allowing us to examine what model assumption can best approximate the specific atmosphere of our target. Our extensive forward-modeling analysis suggests the presence of disequilibrium chemistry, a diabatic thermal structure, clouds, a subsolar metallicity, and a subsolar or near-solar carbon-to-oxygen ratio (C/O) in the atmosphere of COCONUTS-2b (Section 5).

2. Near-Infrared Spectroscopy with Gemini/FLAMINGOS-2

We acquired near-infrared spectra of COCONUTS-2b using the FLAMINGOS-2 (F2) spectrograph (S. S. Eikenberry et al. 2004; S. Eikenberry et al. 2008) on the 8.1 m Gemini-South

¹⁰ <https://www.exoplanetes.umontreal.ca/banyan/banyansigma.php>

¹¹ The mass and companion-to-host mass ratio of COCONUTS-2b are determined by this work (Section 5.4), updated from the values reported by Z. Zhang et al. (2021a).

¹² https://www.iau.org/science/scientific_bodies/commissions/F2/info/documents/

¹³ Here, we use the trigonometric distance of the parent star as the distance of this system, given the consistency in the parallax between COCONUTS-2b (97.9 ± 6.7 mas; J. D. Kirkpatrick et al. 2019) and COCONUTS-2A (91.826 ± 0.019 mas; Gaia Collaboration et al. 2016, 2021).

telescope (GS-2021B-FT-111, GS-2021B-FT-204). The adaptive optics system was not needed because this planet is widely separated from its host star ($594''$) and neighboring detectable sources (mostly $> 20''$ except for one object at $8''$ with comparable *J*-band fluxes). Thirty 200 s frames were taken with the *JH* grism ($0.98\text{--}1.80 \mu\text{m}$) on 2021 December 16 UT, and 36 180 s frames were obtained with the *HK* grism ($1.29\text{--}2.51 \mu\text{m}$) on 2021 December 19 UT and 23 UT. Data were all collected under photometric conditions using the 2 pixel wide slit ($0.''36 \times 263''$) and an ABBA nodding pattern, resulting in an average spectral resolution of $R \sim 900$ (with a maximum of $R \sim 1200$). The A0V telluric standard stars HIP 43762 (on 2021 December 16 and 23) and HIP 28680 (on 2021 December 19) were observed contemporaneously with COCONUTS-2b with airmass differences of 0.01–0.07.

Data reduction was performed using the Gemini IRAF package following the standard procedures, including dark subtraction, flat-fielding, bad-pixel masking, wavelength calibration, one-dimensional spectral extraction, telluric correction, and correction of the detector's sensitivity.¹⁴ In particular, the spectra of COCONUTS-2b were extracted using the traces of the corresponding telluric standard stars as references. This approach allows for more reliable spectral extraction, especially for T/Y dwarfs, whose spectra appear as dashes on the detector (due to the strong H_2O and CH_4 absorption in these objects' atmospheres) and cannot be traced along the full wavelengths (e.g., S. K. Leggett et al. 2016a). Our telluric standard stars were also used to derive the sensitivity function of the detector. We scaled and combined the *JH* and *HK* spectra by aligning their weighted average fluxes near the *H*-band peak ($1.567\text{--}1.602 \mu\text{m}$). The required scaling factor for the *HK* spectrum observed on December 19 and 23 is about 0.87 and 1.73, respectively. The resulting $1.0\text{--}2.5 \mu\text{m}$ spectrum (Z. Zhang et al. 2024b; in vacuum wavelengths) was flux-calibrated using $J_{\text{MKO}} = 19.342 \pm 0.048$ mag (J. D. Kirkpatrick et al. 2011) and the corresponding filter response curve and zero-point flux from A. T. Tokunaga et al. (2002). Figure 2 presents the $1\text{--}25 \mu\text{m}$ spectral energy distribution (SED) of COCONUTS-2b, including our Gemini/F2 spectrum and the WISE, CatWISE, and Spitzer/IRAC photometry (J. D. Kirkpatrick et al. 2011; P. R. M. Eisenhardt et al. 2020; R. M. Cutri et al. 2021; F. Marocco et al. 2021). In Appendix A, we compare our Gemini/F2 spectrum with an archival spectrum (J. D. Kirkpatrick et al. 2011) and the *Y/J/H/K* broadband photometry.

3. A Refined Spectral Type

We updated the spectral type of COCONUTS-2b by comparing its Gemini/F2 spectrum with 209 T0–Y1 ultracool dwarf templates. These ultracool dwarfs were first selected from the UltracoolSheet (W. M. J. Best et al. 2024a) based on spectral types. Binaries or candidate binaries (as suggested by their peculiar spectral morphology) with unresolved spectrophotometry were excluded. We then collected the published spectra of these objects from the literature. Most spectral templates near the T/Y transition were observed by HST/WFC3 ($R \sim 130\text{--}210$; A. C. Schneider et al. 2015); the remaining templates are from IRTF/SpeX ($R \sim 80\text{--}200$; e.g., A. J. Burgasser 2014; W. M. J. Best et al. 2015).

¹⁴ https://gemini-iraf-flamingos-2-cookbook.readthedocs.io/en/latest/Tutorial_Longslit.html

To perform the comparison, we downgraded the resolution of COCONUTS-2b's spectrum, scaled the fluxes of each spectral template following Equation (2) of M. C. Cushing et al. (2008), and computed the reduced χ^2 statistics. This comparison was performed over wavelengths of $1.05\text{--}1.12 \mu\text{m}$, $1.18\text{--}1.33 \mu\text{m}$, and $1.52\text{--}1.66 \mu\text{m}$. Fluxes from wavelengths shorter than $1.05 \mu\text{m}$ were masked to avoid the low sensitivity area near the edge of Gemini/F2's detector; the flux valleys among the *Y/J/H* peaks were masked due to the residuals from telluric correction and the relatively large flux uncertainties of the Gemini/F2 spectrum; fluxes beyond $1.65 \mu\text{m}$ were masked considering the wavelength coverage of HST/WFC3 spectral templates.

As shown in Figure 3, the five best-matched templates to COCONUTS-2b's spectrum are WISEA J221216.27–693121.6 (T9.5; A. C. Schneider et al. 2015), WISE J154214.00 + 223005.2 (T9.5; G. N. Mace et al. 2013), WISE J073444.02 – 715744.0 (Y0; J. D. Kirkpatrick et al. 2012), WISE J222055.31 – 362817.4 (Y0; J. D. Kirkpatrick et al. 2012), and UGPS J072227.51 – 054031.2 (T9; P. W. Lucas et al. 2010). The near-infrared spectra of the first four objects and the last one were obtained by A. C. Schneider et al. (2015) and M. C. Cushing et al. (2011), respectively. Consequently, we assign a new spectral type of $T9.5 \pm 0.5$ to COCONUTS-2b.

4. Forward-modeling Analysis of COCONUTS-2b

We compare the spectrophotometry of COCONUTS-2b with 16 state-of-the-art atmospheric model grids, precomputed with various assumptions about the atmospheres of T/Y dwarfs. Each model grid is utilized over its entire regular parameter space when possible, with an upper limit of 800 K in the effective temperature (T_{eff}).

4.1. Atmospheric Model Grids

4.1.1. ATMO2020

The ATMO2020 atmospheric models¹⁵ were developed by M. W. Phillips et al. (2020), assuming radiative-convective equilibrium, solar metallicity, and cloud-free atmospheres. These models incorporate recent line profiles for the potassium resonance doublet (N. F. Allard et al. 2016) that shape the spectra of T and Y dwarfs in the red optical and *Y* band (e.g., Figure 2). The grid parameters include T_{eff} and logarithmic surface gravity ($\log(g)$).¹⁶ ATMO2020 includes a set of rainout chemical equilibrium models (ATMO2020 CEQ), and two sets of chemical disequilibrium models with weak (ATMO2020 NEQ weak) and strong (ATMO2020 NEQ strong) vertical mixing. The mixing is quantified by the eddy diffusion coefficient K_{zz} , assumed to vary from $10^{10} \text{ cm}^2 \text{ s}^{-1}$ or $10^8 \text{ cm}^2 \text{ s}^{-1}$ at $\log(g) = 2.5$ dex to $10^4 \text{ cm}^2 \text{ s}^{-1}$ or $10^2 \text{ cm}^2 \text{ s}^{-1}$ at $\log(g) = 5.5$ dex for the strong and weak cases, respectively; the K_{zz} is assumed to be constant with pressures. Our forward-modeling analysis uses all three versions of the grids with $T_{\text{eff}} \in [200, 800]$ K and $\log(g) \in [2.5, 5.5]$ dex.

4.1.2. ATMO2020++ and PH_3 -free ATMO2020++

By expanding the ATMO2020 framework (M. W. Phillips et al. 2020), S. K. Leggett et al. (2021) and A. M. Meisner et al. (2023)

¹⁵ Available via the ERC-ATMO Opendata website maintained by P. Tremblin: <https://noctis.erc-atmo.eu/fsdownload/zyU96xA6o/phillips2020>.

¹⁶ Throughout this manuscript, we use “ $\log()$ ” and “ $\ln()$ ” for 10-based and natural logarithm, respectively.

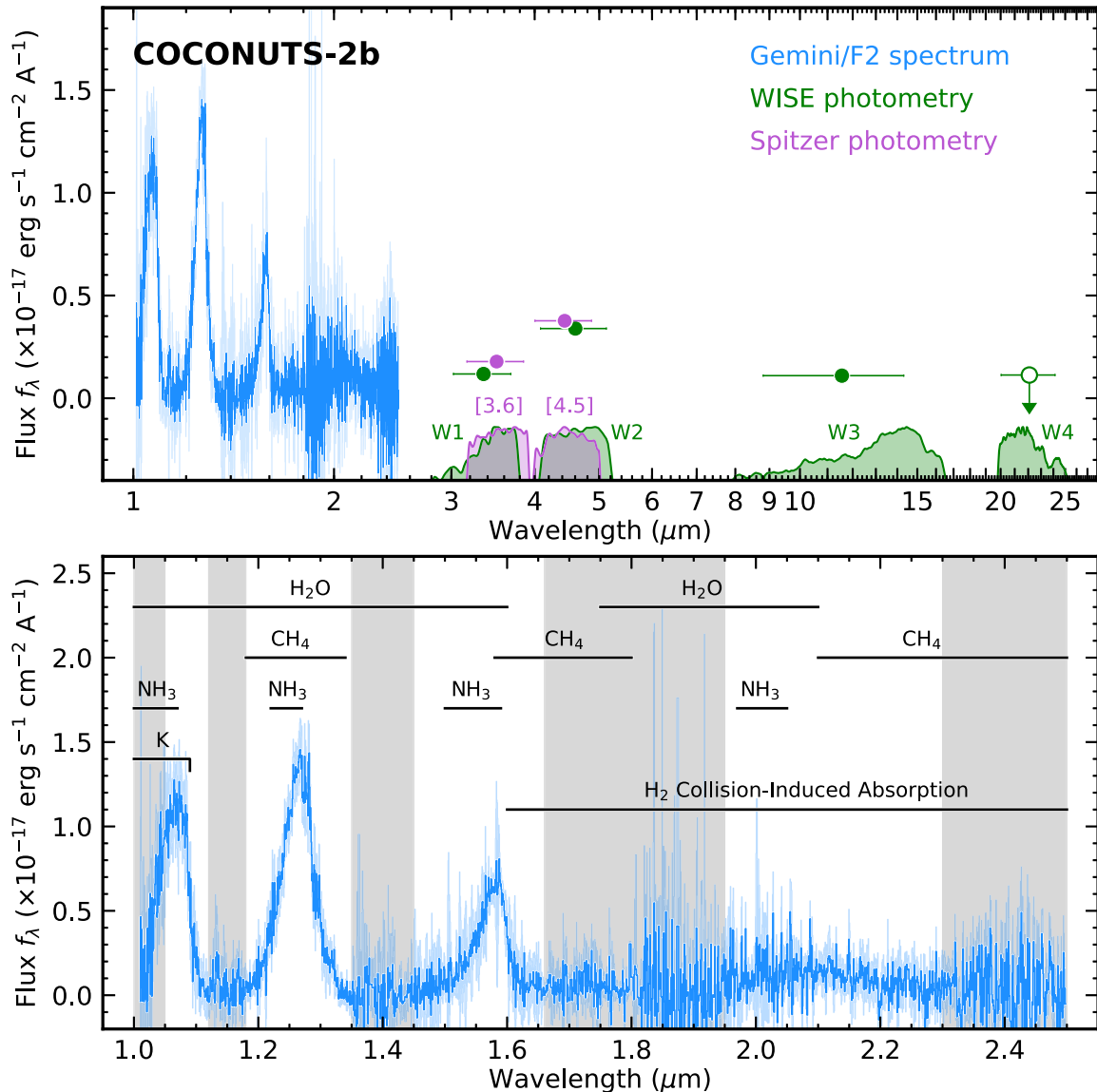


Figure 2. Top panel: The 1–25 μm SED of COCONUTS-2b, including our new Gemini/F2 spectrum (blue) and the WISE (green) and Spitzer (purple) photometry. This object's W1 and W2 photometry are from CatWISE, with proper motion accounted for; the W4 photometry is an upper limit. The spectral flux uncertainties are shown as light shades. Bottom panel: The Gemini/F2 spectrum with key spectral features labeled. Fluxes in gray shades are masked for the subsequent forward-modeling analysis in Section 4.

developed the ATMO2020++ models,¹⁷ which additionally incorporate a nonadiabatic thermal structure in the atmospheres. Such a diabatic process has been suggested by studies of solar system gas-giant planets and brown dwarfs (e.g., T. Guillot et al. 1994; P. Tremblin et al. 2015; S. K. Leggett et al. 2017; P. Tremblin et al. 2019; S. K. Leggett & P. Tremblin 2023; S. Petrus et al. 2023). The ATMO2020++ models are obtained by tuning the adiabatic index γ (≈ 1.4 for pure molecular hydrogen gas) of the ATMO2020 NEQ strong models until the predicted emission spectra qualitatively match the observed data of a handful of T/Y brown dwarfs. The modified adiabatic index can reduce the temperature gradient of the atmospheric temperature-pressure profile (Section 5.1). The publicly available grid assumes the adiabatic temperature-pressure profile in the deep atmosphere, with a tuned $\gamma = 1.25$

for pressures below 15 bar. The grid parameters of ATMO2020 ++ include T_{eff} , $\log(g)$, and metallicity ([M/H]) at solar and subsolar values. We use the models with $T_{\text{eff}} \in [250, 800] \text{ K}$, $\log(g) \in [2.5, 5.5] \text{ dex}$, and [M/H] values of -1.0 dex , -0.5 dex , 0 dex , and $+0.3 \text{ dex}$.

Building upon the ATMO2020++ grid, S. K. Leggett & P. Tremblin (2024) published the PH₃-free ATMO2020++ grid.¹⁸ The assumptions of these two model grids are kept the same, except that the latter does not include phosphine, as inspired by the JWST observations of late-T and Y brown dwarfs (e.g., S. A. Beiler et al. 2023; S. K. Leggett & P. Tremblin 2023; K. L. Luhman et al. 2024). We use the models with $T_{\text{eff}} \in [250, 800] \text{ K}$, $\log(g) \in [4.0, 5.0] \text{ dex}$, and [M/H] values of -0.5 dex , 0 dex , and $+0.3 \text{ dex}$.

¹⁷ Available via the ERC-ATMO Opendata website maintained by P. Tremblin: <https://noctis.erc-atmo.eu/fsdownload/Q7MUSoCLR/meisner2023>.

¹⁸ Available via the ERC-ATMO Opendata website maintained by P. Tremblin: <https://noctis.erc-atmo.eu/fsdownload/9puhIZma2/leggett2024>.

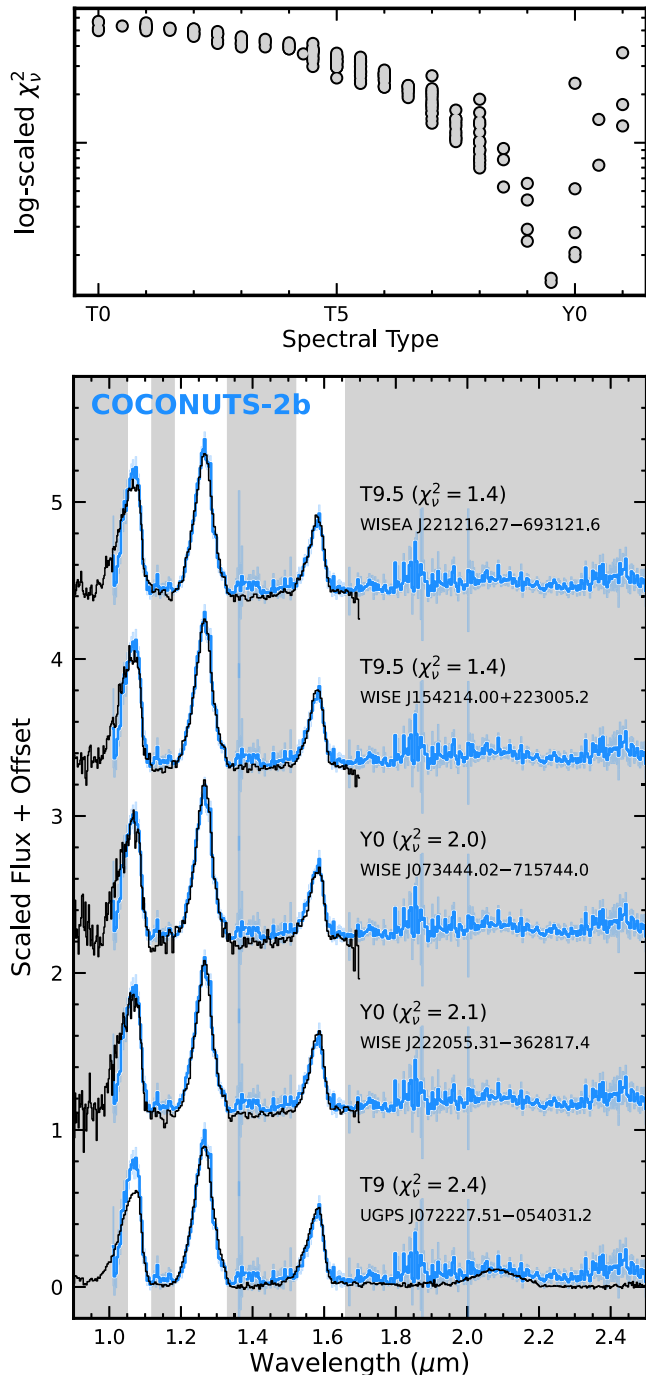


Figure 3. Top panel: Reduced χ^2 values of the fitted T0–Y1 spectral templates. The best-matched template with the lowest χ^2_ν has a T9.5 spectral type. Bottom panel: The Gemini/F2 spectrum of COCONUTS-2b (blue; with downgraded spectral resolution) overlaid with five best-fitted spectral templates (black). The masked wavelength ranges in this comparison are highlighted in gray shades, which are different from the gray shades shown in Figure 2.

4.1.3. Sonora Bobcat and Sonora Elf Owl

The Sonora Bobcat models¹⁹ were developed by M. S. Marley et al. (2021b), assuming radiative-convective equilibrium, rainout equilibrium chemistry, and cloud-free atmospheres. A dedicated comparative analysis between these models and a large spectroscopic data set was performed by

Z. Zhang et al. (2021b) and Z. Zhang et al. (2021c). They verified that the Sonora Bobcat models could match the spectrophotometry of late-T dwarfs and discussed the systematic offsets between data and models. We use this grid with $T_{\text{eff}} \in [200, 800]$ K, $\log(g) \in [3.25, 5.5]$ dex, and $[\text{M}/\text{H}]$ values of -0.5 dex, 0 dex, and $+0.5$ dex, with the C/O fixed at solar value ($\text{C}/\text{O}_\odot = 0.458$; K. Lodders 2010a).

Within the same model series, the Sonora Elf Owl grid²⁰ was developed by Mukherjee et al. (2024). These models have similar assumptions as Sonora Bobcat but additionally incorporate disequilibrium chemistry and updated alkali opacities (N. F. Allard et al. 2016, 2019) with broader ranges of $[\text{M}/\text{H}]$ and C/O. Our analysis focuses on the models with $T_{\text{eff}} \in [200, 800]$ K, $\log(g) \in [3.25, 5.5]$ dex, $[\text{M}/\text{H}] \in [-0.5, +0.5]$ dex, C/O $\in [0.22, 1.14]$, and (the pressure-independent) $K_{zz} \in [10^2, 10^9] \text{ cm}^2 \text{s}^{-1}$.

4.1.4. C. V. Morley et al. (2012) and C. V. Morley et al. (2014)

While the aforementioned model grids assume cloud-free atmospheres, C. V. Morley et al. (2012) proposed that optically thin clouds (e.g., KCl, Na₂S, ZnS, MnS, and Cr) form in T and Y dwarf atmospheres, impacting their thermal emission spectra (also see K. Lodders 1999; M. Marley 2000; A. Burrows et al. 2001; J. J. Fortney 2005). Compared to cloud-free models, the predictions of their cloudy models are more consistent with the observed near-infrared photometry of mid-to-late-T dwarfs. The C. V. Morley et al. (2012) models (Morley12)²¹ assume radiative-convective equilibrium, rainout equilibrium chemistry, and solar metallicity, parameterized by T_{eff} , $\log(g)$, and the condensate sedimentation efficiency f_{sed} (A. S. Ackerman & M. S. Marley 2001). We use the models with $T_{\text{eff}} \in [400, 800]$ K, $\log(g) \in [4.0, 5.5]$ dex, $f_{\text{sed}} \in [2, 5]$.

C. V. Morley et al. (2014)²² expanded these C. V. Morley et al. (2012) models toward colder effective temperatures and incorporated the formation of water ice clouds with an inhomogeneous cloud cover (Morley14; also see M. S. Marley et al. 2010). Our analysis uses the models with $T_{\text{eff}} \in [200, 450]$ K, $\log(g) \in [3.0, 5.0]$ dex, a fixed $f_{\text{sed}} = 5$, and a fixed cloud patchiness of 50%.

4.1.5. E. F. Linder et al. (2019)

E. F. Linder et al. (2019) developed atmospheric models with radiative-convective equilibrium, equilibrium chemistry, and assumptions of both cloud-free (Linder19 Clear) and cloudy (Linder19 Cloudy) atmospheres.²³ This grid is an extension of the models developed by M. Samland et al. (2017) when studying the directly imaged exoplanet 51 Eri b using petitCODE (P. Mollière et al. 2017). The cloudy models incorporate the formation of Na₂S and KCl condensates; as noted by E. F. Linder et al. (2019), these models ignore water ice clouds that are important for T_{eff} below 400 K (e.g., C. V. Morley et al. 2014; B. Lacy & A. Burrows 2023a). We

²⁰ On Zenodo—Y-type models: S. Mukherjee et al. (2023a), T-type models: S. Mukherjee et al. (2023b), L-type models: S. Mukherjee et al. (2023c) was developed by S. Mukherjee et al. (2024).

²¹ Available via the website www.carolinemorley.com/models maintained by C. Morley: <https://www.dropbox.com/s/3ln7pyitueor2r/sulfideclouds.tar.gz>.

²² Available via the website www.carolinemorley.com/models maintained by C. Morley: https://www.dropbox.com/s/djdm8k8rl1dvvm/spectra_Morley2014.zip?dl=0.

²³ Available via the website of P. Mollière: http://mpia.de/~molliere/online_data/linder_molliere_grid.zip.

¹⁹ On Zenodo—M. S. Marley et al. (2021a).

use both cloud-free and cloudy models with $T_{\text{eff}} \in [300, 800]$ K, $\log(g) \in [1.5, 5.0]$ dex, $[\text{M}/\text{H}] \in [-0.4, +1.4]$ dex, and $f_{\text{sed}} \in [0.5, 3.0]$ (for cloudy models).

4.1.6. B. Lacy & A. Burrows (2023a)

B. Lacy & A. Burrows (2023a) developed new atmospheric models for Y dwarfs assuming radiative-convective equilibrium, along with the updated opacities of alkali lines (N. F. Allard et al. 2016, 2019), among others. These models include assumptions of both cloud-free and cloudy atmospheres, and both equilibrium and disequilibrium chemistry, leading to four versions in total (LB23 Clear/Cloudy CEQ/NEQ).²⁴ For NEQ models, the K_{zz} is calculated as a function of pressures based on the mixing length theory in the convective zone and is fixed at $10^6 \text{ cm}^2 \text{ s}^{-1}$ in the radiative zone. We use the cloud-free CEQ and NEQ models with $T_{\text{eff}} \in [200, 600]$ K, $\log(g) \in [3.5, 5.0]$ dex, and $[\text{M}/\text{H}]$ values of -0.5 dex, 0 dex, and $+0.5$ dex.

The cloudy models include a homogeneous water ice cloud cover, with opacities modulated by the vertical extent and characteristic cloud particle size. These models include a regular grid with $T_{\text{eff}} \in [250, 400]$ K, $\log(g) \in [4.0, 5.0]$ dex, and $[\text{M}/\text{H}]$ values of -0.5 dex and 0 dex, along with a few irregularly spaced models at $T_{\text{eff}} = 450$ K. Given that the maximum T_{eff} of the regular grid is too cold for COCONUTS-2b, we do not include these cloudy models in the forward-modeling analysis presented in Section 4.3. Instead, we compare these models with the Gemini/F2 spectrum of COCONUTS-2b based on χ^2 , as detailed in Appendix B.

4.1.7. Exo-REM

The Exo-REM atmospheric models (J. L. Baudino et al. 2015; B. Charnay et al. 2018; D. Blain et al. 2021)²⁵ assume radiative-convective equilibrium and incorporate disequilibrium chemistry using the self-consistently calculated K_{zz} -pressure profiles. The publicly available grid includes iron and silicate clouds with simple microphysics. The Na₂S, KCl, and water condensates, which are important for the atmospheres of T/Y dwarfs (e.g., C. V. Morley et al. 2012, 2014), are not implemented by these models. Nevertheless, within the Exo-REM framework, the effects of iron and silicate clouds are notable near the T/Y transition at low surface gravities (Section 5.1). Our analysis uses the models with $T_{\text{eff}} \in [400, 800]$ K, $\log(g) \in [3.0, 5.0]$ dex, C/O $\in [0.1, 0.8]$, and $[\text{M}/\text{H}]$ values of -0.5 dex, 0 dex, $+0.5$ dex, and $+1.0$ dex.

4.2. Methodology

We constrain the physical properties of COCONUTS-2b by comparing each model grid to its Gemini/F2 spectrum and W1, W2, [3.6], and [4.5] photometry. For the analysis presented in this section, we exclude the W3 and W4 (upper limit) magnitudes because the Sonora Elf Owl models do not cover the filter response curves of these two bands. As discussed in Section 5.3, our analysis results and conclusions are not significantly altered when W3 is included. Upcoming JWST NIRSPEC and MIRI spectroscopy (GO 2124, GO 3514, GO 6463) will provide more insights into this object's appearance and properties in the mid-infrared. Additionally,

our analysis uses the Gemini/F2 spectrum in the wavelength ranges of $1.05\text{--}1.12 \mu\text{m}$, $1.18\text{--}1.35 \mu\text{m}$, $1.45\text{--}1.66 \mu\text{m}$, and $1.95\text{--}2.30 \mu\text{m}$ (see Figure 2). The lower wavelength cut of $1.05 \mu\text{m}$ is determined considering the flux drop of the Gemini/F2 data when compared with spectral templates (Section 3).

We perform the forward-modeling analysis using the nested sampling algorithm PyMultiNest (F. Feroz & M. P. Hobson 2008; F. Feroz et al. 2009; J. Buchner et al. 2014; F. Feroz et al. 2019), with 4000 live points and a 0.8 sampling efficiency. The fitting process terminates once the change in the natural logarithmic evidence between iterations drops below 0.5. The free parameters include the model grid parameters, radius (R), and a hyper-parameter accounting for any underestimated flux uncertainties of our Gemini/F2 spectrum, described in a logarithmic scale ($\log(b)$). Uniform priors are adopted for all these parameters. The grid parameters are constrained within the ranges described in Section 4.1; R is constrained between $0.5 R_{\text{Jup}}$ and $2.5 R_{\text{Jup}}$; and the boundaries of $\log(b)$ correspond to a range from 10% of the minimum Gemini/F2 spectral flux uncertainty to 100 times the maximum flux uncertainty over the fitted wavelength range (i.e., $2.2 \times 10^{-20}\text{--}8.2 \times 10^{-16} \text{ erg s}^{-1} \text{ cm}^{-2} \text{ \AA}^{-1}$).

The model spectra are interpolated to a given set of grid parameters. This interpolation is performed in logarithmic scales for T_{eff} , K_{zz} , and fluxes, and in linear scales for $\log(g)$, $[\text{M}/\text{H}]$, f_{sed} , and C/O. The interpolated models are then scaled by $(R/d)^2$, with $d = 10.888$ pc fixed at the planet-host star's distance (C. A. L. Bailer-Jones et al. 2021). Log-likelihood is evaluated via

$$\ln \mathcal{L} = \ln \mathcal{L}_{\text{spec}} + \ln \mathcal{L}_{\text{phot}} \quad (1)$$

where

$$\begin{aligned} \ln \mathcal{L}_{\text{spec}} &= -\frac{1}{2} \sum_i^{N_{\text{pix}}} \frac{(\mathcal{F}_{\text{obs},i} - \mathcal{F}_{\text{mod},i})^2}{\sigma_{\text{obs},i}^2 + b^2} - \frac{1}{2} \ln [2\pi(\sigma_{\text{obs},i}^2 + b^2)] \\ \ln \mathcal{L}_{\text{phot}} &= -\frac{1}{2} \sum_j^{N_{\text{phot}}} \frac{(\mathcal{F}_{\text{obs},j} - \mathcal{F}_{\text{mod},j})^2}{\sigma_{\text{obs},j}^2} - \frac{1}{2} \ln [2\pi(\sigma_{\text{obs},j}^2)]. \end{aligned} \quad (2)$$

Here, \mathcal{F}_{obs} and σ_{obs} represent the observed flux and uncertainty of spectrophotometry, N_{pix} is the total number of spectral wavelength pixels, and $N_{\text{phot}} = 4$ is the number of broadband photometry. For photometric data, the predicted model flux, \mathcal{F}_{mod} , is calculated using the filter response curves (J. L. Hora et al. 2008; T. H. Jarrett et al. 2011).

4.3. Results

We perform forward-modeling analysis for COCONUTS-2b using the atmospheric model grids described in Section 4.1. These models are categorized based on their assumptions:

1. Models with disequilibrium chemistry, diabatic atmospheric thermal structure, and no clouds: ATMO2020++ and PH₃-free ATMO2020++.
2. Models with disequilibrium chemistry and clouds: Exo-REM and LB23 Cloudy NEQ.
3. Models with disequilibrium chemistry and no clouds: ATMO2020 NEQ weak, ATMO2020 NEQ strong, Sonora Elf Owl, and LB23 Clear NEQ.

²⁴ On Zenodo—B. Lacy & A. Burrows (2023b).

²⁵ https://lesia.obspm.fr/exorem/YPG_grids/

4. Models with equilibrium chemistry and clouds: Morley12, Morley14, Linder19 Cloudy, and LB23 Cloudy CEQ.
5. Models with equilibrium chemistry and no clouds: ATMO2020 CEQ, Sonora Bobcat, Linder19 Clear, and LB23 Clear CEQ.

The bolometric luminosity of COCONUTS-2b is estimated using the inferred T_{eff} and R posteriors:

$$L_{\text{bol}} = 4\pi R^2 \sigma_{\text{SB}} T_{\text{eff}}^4 + 4\pi d^2 \int_{\Lambda} (\mathcal{F}_{\lambda,\text{obs}} - \langle \mathcal{F}_{\lambda,\text{mod}} \rangle) d\lambda. \quad (3)$$

Here, σ_{SB} is the Stefan–Boltzmann constant, d is the distance of COCONUTS-2b, and Λ represents the wavelength ranges used in the forward-modeling analysis, i.e., 1.05–1.12 μm , 1.18–1.35 μm , 1.45–1.66 μm , and 1.95–2.30 μm . The second term in Equation (3) accounts for any discrepancies between the observed fluxes and the fitted model spectra. Specifically, $(\mathcal{F}_{\lambda,\text{obs}} - \langle \mathcal{F}_{\lambda,\text{mod}} \rangle)$ represents the residuals between the observed Gemini/F2 spectrum and the maximum-likelihood model spectrum. Our error propagation of L_{bol} accounts for the observed flux uncertainties and the best-fitted hyper-parameter b (Section 4.2).

The spectroscopically inferred mass of COCONUTS-2b can be computed for each model grid based on $\log(g)$ and R , but these values are not explicitly reported in this work. These spectroscopically inferred masses should be interpreted with caution, given the known challenges of accurately determining $\log(g)$ and R from thermal emission spectra of gas-giant exoplanets and brown dwarfs (e.g., M. C. Cushing et al. 2008; D. C. Stephens et al. 2009; M. C. Liu et al. 2011; M. R. Line et al. 2017; J. A. Zalesky et al. 2019; E. C. Gonzales et al. 2020; Z. Zhang et al. 2021b, 2021c; A. Lueber et al. 2022; C. E. Hood et al. 2023; Z. Zhang et al. 2023a).

We compute the Bayesian information criterion (BIC; G. Schwarz 1978; A. R. Liddle 2007) for each model grid as follows:

$$\text{BIC} \equiv -2 \ln \mathcal{L}_{\text{max}} + k \ln N \quad (4)$$

where \mathcal{L}_{max} is the maximum likelihood, k is the number of free parameters, and N is the number of data points. As proposed by R. E. Kass & A. E. Raftery (1995), a model with a BIC that is lower by more than 6 compared to another model is strongly preferred for interpreting the observations. If the ΔBIC between the two models is less than 2, the preference is not considered significant. With this metric as guidance, we visually examine data-model discrepancies to evaluate the various model assumptions.

Figures 4–8 present our results, with confidence intervals of the inferred parameters summarized in Table 1. We compute a ΔBIC value for each model grid by comparing its BIC with that of the most preferred grid, PH_3 -free ATMO2020++; a corner plot of the inferred parameters from this grid is shown in Figure 9. Results for the LB23 Cloudy CEQ and NEQ models are skipped in this section because their inferred T_{eff} posteriors are pinned at the upper boundary of 400 K, which is too cold for COCONUTS-2b. In Appendix B, we present the χ^2 -based spectral fitting analyses of COCONUTS-2b using these models.

5. Discussion

5.1. Disequilibrium Chemistry, Diabatic Thermal Structure, and Clouds of COCONUTS-2b

Among all the model grids, PH_3 -free ATMO2020++, ATMO2020++, and Exo-REM are preferred for matching the observed spectrophotometry of COCONUTS-2b because they yield the lowest BIC values (Figures 4–5). These grids incorporate disequilibrium chemistry and additional atmospheric processes—diabatic thermal structure or clouds—that are not the assumptions of the remaining models.

The PH_3 -free ATMO2020++ and ATMO2020++ model grids are expansions of ATMO2020 NEQ strong, with a modified adiabatic index (Section 4.1.2). This modification was motivated and guided by discrepancies between ATMO2020 NEQ strong and the observed spectrum of UGPS J072227.51 –054031.2 (the fifth best-matched single spectral template of COCONUTS-2b; Figure 3) in the J , K , and [3.6] bands (see Section 5.1 of S. K. Leggett et al. 2021). Therefore, it is not surprising that these models are preferred against other standard disequilibrium cloud-free models. With a modified $\gamma = 1.25$, the atmospheric thermal structure becomes slightly hotter than the standard case in the upper atmosphere, where the W_1 , W_2 , [3.6], and [4.5] fluxes are emitted, and slightly colder in the deep atmosphere, where the Y , J , and H fluxes are emitted (e.g., S. K. Leggett et al. 2021). This is equivalent to a reduced temperature gradient of the temperature–pressure profile. The resulting emission spectra appear slightly redder in the near-infrared wavelengths, similar to the effects of cloud opacities, even though these models do not include clouds. This prescribed γ modification may be interpreted in the context of the thermo-compositional convection triggered by the transitions of $\text{CO} \rightleftharpoons \text{CH}_4$ and $\text{N}_2 \rightleftharpoons \text{NH}_3$, the breaking of gravity waves, chromospheric activity, latent heating during condensation, or non-one-dimensional dynamics in the atmospheres (e.g., S. Sorahana et al. 2014; P. Tremblin et al. 2015; J. O’Donoghue et al. 2016; P. Tremblin et al. 2019; S. K. Leggett et al. 2021; S.-Y. Tang et al. 2021). The diabatic atmospheric thermal structure has also been suggested in the atmospheres of other late-T and Y dwarfs based on forward models or atmospheric retrievals (e.g., S. K. Leggett et al. 2016a, 2017, 2019, 2021; J. A. Zalesky et al. 2019; S. K. Leggett & P. Tremblin 2023, 2024; A. M. Meisner et al. 2023; K. L. Luhman et al. 2024).

The Exo-REM model grid yields a ΔBIC of 111 (Table 1), meaning that it is disfavored compared to the PH_3 -free ATMO2020++ and ATMO2020++ models. Nevertheless, Exo-REM is preferred among all the model grids with the standard γ . The Exo-REM models used in this study incorporate iron and silicate clouds (B. Charnay et al. 2018). These cloud species are crucial for gas-giant planets and brown dwarfs near the L/T transition (e.g., K. Lodders & B. J. Fegley 2006; M. S. Marley & T. D. Robinson 2015). In colder atmospheres of late-T and Y dwarfs, iron and silicate clouds condense below or near the bottom of the near-infrared photospheres. The primary cloud species at the T/Y transition include KCl , Na_2S , and water (e.g., C. V. Morley et al. 2012, 2014), which are not included by the public Exo-REM models. However, within the Exo-REM framework, the iron and silicate clouds still impact the emergent spectra at low effective temperatures when surface gravities are low. Figure 10 compares Exo-REM model spectra with and without clouds; the spectral resolutions of these models ($R \sim 500$) are

disequilibrium chemistry + diabatic T-P + no clouds

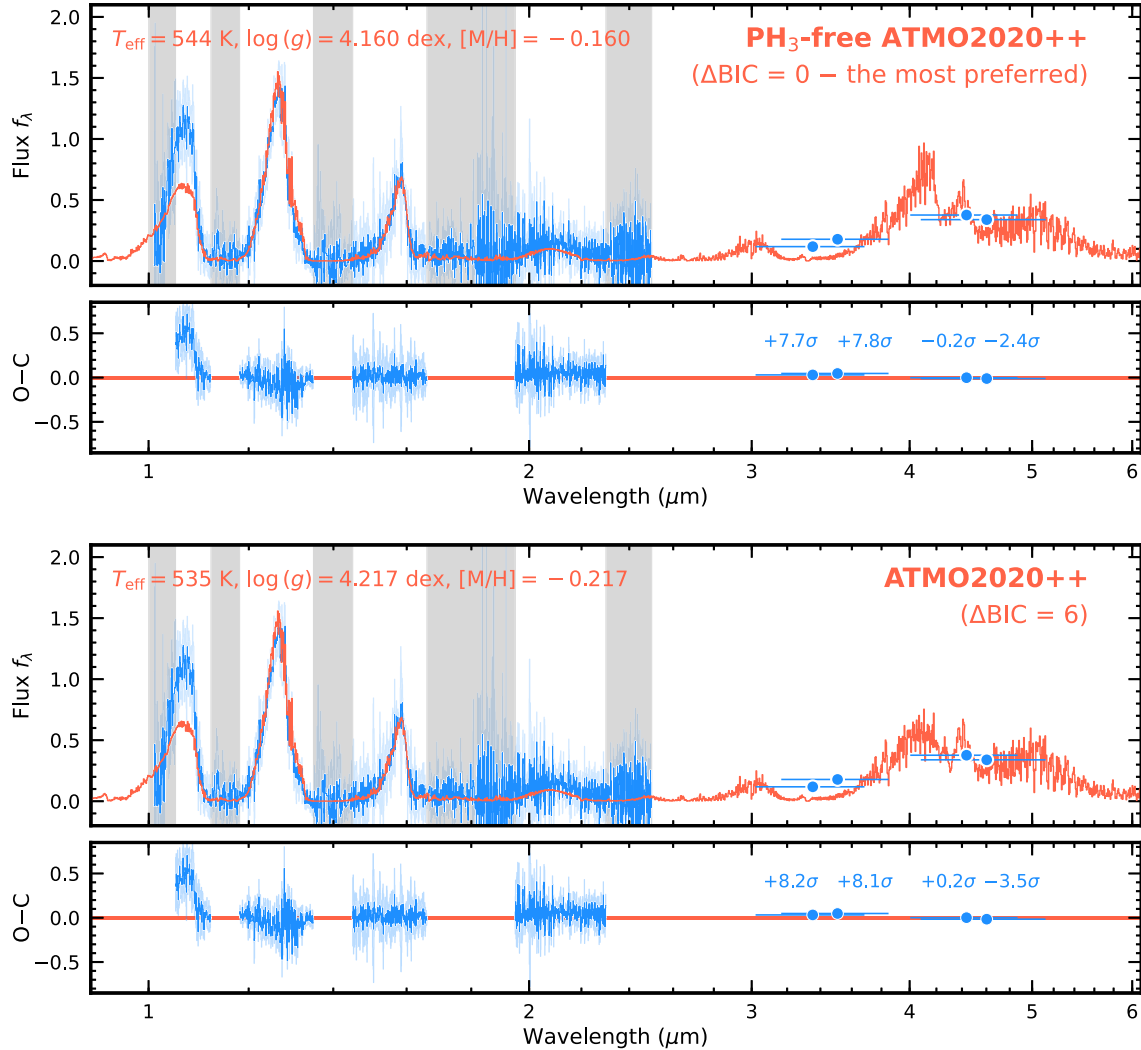


Figure 4. Forward-modeling results based on models with disequilibrium chemistry, diabatic temperature–pressure (T – P) profiles, and no clouds. For each grid, the observed spectrophotometry of COCONUTS-2b (blue) and the maximum-likelihood model spectrum (orange) are plotted in the top panel; the best-fit T_{eff} , $\log(g)$, and $[\text{M}/\text{H}]$ values are labeled. The gray-shaded regions indicate the masked wavelengths in the forward-modeling analysis. The bottom panel shows the data–model residuals, with the significance values labeled for the broadband photometry. The unit of plotted fluxes is $10^{-17} \text{ erg s}^{-1} \text{ cm}^{-2} \text{ \AA}^{-1}$. The ΔBIC of a given grid is computed relative to the BIC of the PH_3 -free ATMO2020++ results.

lower than those used in our forward-modeling analysis ($R \sim 2 \times 10^4$). Although the spectral effects of iron and silicate clouds weaken at colder effective temperatures, they remain significant at the characteristic T_{eff} values of T/Y dwarfs (e.g., 500 K) when $\log(g) \lesssim 4.0$ dex. Our spectroscopically inferred $T_{\text{eff}} \approx 450$ K and $\log(g) = 3.348^{+0.004}_{-0.006}$ dex (Table 1) indicate that cloud effects are important within the Exo-REM framework. Therefore, our analysis suggests the need for cloud opacities for interpreting COCONUTS-2b’s spectrophotometry when the standard atmospheric adiabatic index is assumed. However, we cannot conclude whether iron and silicate clouds are the predominant cloud species for COCONUTS-2b.

These findings suggest dynamic processes in the atmosphere of COCONUTS-2b, including disequilibrium chemistry, a diabatic thermal structure, and potential clouds (also see Z. Zhang et al. 2021a). Such processes are likely prevalent in the atmospheres of late-T and Y dwarfs, potentially explaining the observed diversity in their spectrophotometry

(e.g., S. K. Leggett et al. 2017; W. M. J. Best et al. 2020; J. D. Kirkpatrick et al. 2021; A. Sanghi et al. 2023). These processes may also lead to top-of-atmosphere inhomogeneity, such as hot/cold spots and patchy clouds (e.g., A. P. Showman & Y. Kaspi 2013; X. Zhang & A. P. Showman 2014; A. P. Showman et al. 2019; X. Tan & A. P. Showman 2019; A. P. Showman et al. 2020; P. Tremblin et al. 2020; X. Tan & A. P. Showman 2021), resulting in rotationally modulated or irregular time-evolving variabilities that can be probed via spectrophotometric monitoring (e.g., É. Artigau et al. 2009; J. Radigan et al. 2014; S. K. Leggett et al. 2016b; Y. Zhou et al. 2016; D. Apai et al. 2017; E. Manjavacas et al. 2019; B. P. Bowler et al. 2020; B. W. P. Lew et al. 2020; J. M. Vos et al. 2022; Y. Zhou et al. 2022; P. Liu et al. 2024). To date, variability measurements for T/Y dwarfs are less extensive than those for objects near the L/T transition. Only a handful of T8–Y2 objects have exhibited variability signals, with amplitudes reaching up to 2.6% in the J band (e.g., E. Manjavacas et al. 2019).

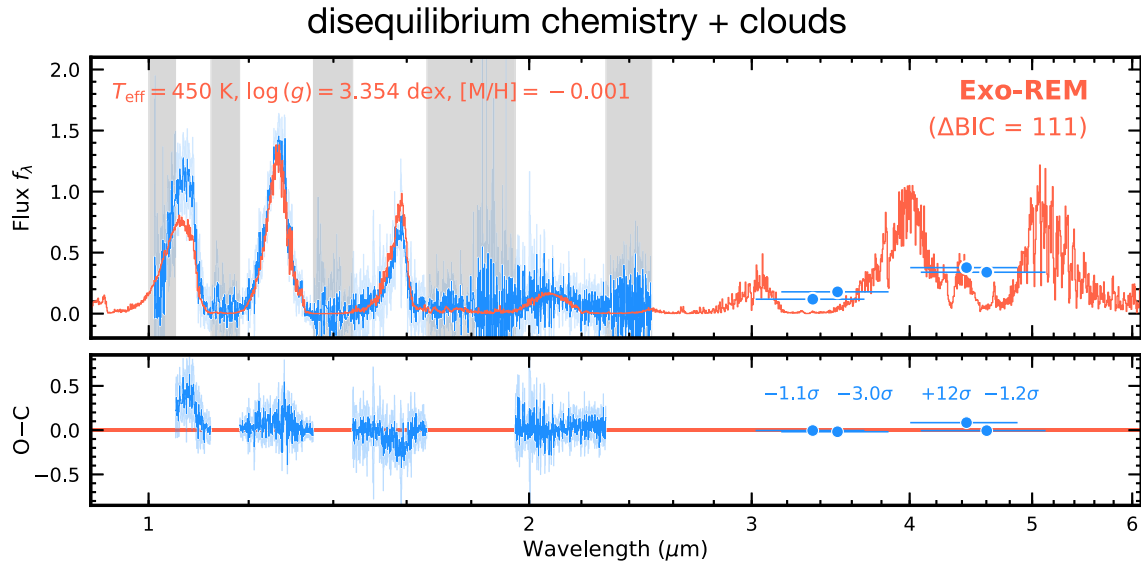


Figure 5. Forward-modeling results based on the Exo-REM models that include disequilibrium chemistry and clouds, with the same format as Figure 4.

or 7.5% near $4.5\text{ }\mu\text{m}$ (e.g., M. C. Cushing et al. 2016; T. L. Esplin et al. 2016; S. K. Leggett et al. 2016b). Variability monitoring of COCONUTS-2b, however, has yet to be reported, especially considering the challenges posed by its faintness ($J=19.342$ mag) in ground-based observations. Space-based observations by, e.g., JWST offer a promising approach for investigating the atmospheric variability of this object.

5.2. Major Discrepancies Between Data and Models

5.2.1. All Model Grids: Underpredicted Fluxes in the Y band

As shown in Figures 4–8, all model grids predict Y -band fluxes that are fainter than the observations by $1\text{--}2\sigma$, regardless of their underlying assumptions. Similar offsets have been observed in forward-modeling analyses of other late-T and Y dwarfs (e.g., J. J. Bochanski et al. 2011; A. C. Schneider et al. 2015; S. K. Leggett et al. 2016a; M. W. Phillips et al. 2020; S. K. Leggett et al. 2021; Z. Zhang et al. 2021c; M. W. Phillips et al. 2024). It has been suggested in the literature that incorporating disequilibrium chemistry may alleviate this offset because vertical mixing can reduce the abundance of NH_3 , which has an absorption feature in the Y band (Figure 2) based on theoretical predictions (e.g., D. Saumon et al. 2012). Indeed, this alone cannot fully explain the Y -band discrepancies observed for COCONUTS-2b because some models used in our analysis already include disequilibrium chemistry (Section 4.1).

The Y -band fluxes of late-T and Y dwarfs are influenced by the pressure-broadened wings of alkali resonance lines in the optical wavelengths (Figure 2). M. W. Phillips et al. (2020) found that the ATMO2020 models, which incorporate the latest opacity database of K (N. F. Allard et al. 2016), yield better data-model consistencies in the Y -band spectrum of the late-T dwarf GJ 570D ($T_{\text{eff}} \approx 786\text{ K}$; Z. Zhang et al. 2021b) compared to models with previous line profiles (N. F. Allard et al. 2003; A. Burrows & M. Volobuyev 2003). Despite this, several model grids in our analysis already incorporate the latest opacities of Na (N. F. Allard et al. 2019) and/or K (N. F. Allard et al. 2016), suggesting that the alkali opacities

are likely not the primary source of the persistent Y -band offsets across the model grids.

The Y -band data-model offsets may be attributed to uncertainties in alkali chemistry models, including the condensation and rainout of Na and K. M. W. Phillips et al. (2020) noted that reducing the K abundance by nearly an order of magnitude in the ATMO2020 models could resolve the Y -band data-model differences seen in other Y dwarfs. Additionally, alkali rainout was also suggested by atmospheric retrievals performed for large ensembles of late-T and Y dwarfs (e.g., M. R. Line et al. 2017; J. A. Zalesky et al. 2019, 2022).

5.2.2. Most Model Grids: Underpredicted Fluxes near $3.6\text{ }\mu\text{m}$

All model grids, except Exo-REM, predict fainter fluxes than the observations at the wavelengths of W1 and [3.6] photometry (Figure 4–8), with significance values of $4\sigma\text{--}22\sigma$. These data-model offsets near $3.6\text{ }\mu\text{m}$, as influenced by the CH_4 absorption, are sometimes connected with departures from equilibrium chemistry. The disequilibrium chemistry occurs when the timescale for vertical mixing is shorter than that of the $\text{CO} \rightarrow \text{CH}_4$ chemical reaction (e.g., R. G. Prinn & S. S. Barshay 1977; B. J. Fegley & K. Lodders 1996; D. Saumon et al. 2000; K. J. Zahnle & M. S. Marley 2014; P. Tremblin et al. 2015; B. E. Miles et al. 2020; T. Karalidi et al. 2021; S. Mukherjee et al. 2023, 2024). Vertical mixing quenches the CH_4 abundance in the deep atmosphere, leading to an overabundance of CO relative to CH_4 . However, the offsets near $3.6\text{ }\mu\text{m}$ are present in both chemical equilibrium and disequilibrium models, indicating that additional factors may be involved.

S. K. Leggett et al. (2021) proposed that upper-atmospheric heating could enhance the model-predicted fluxes near $3.6\text{ }\mu\text{m}$ and improve the data-model consistency for late-T and Y dwarfs. With a modified adiabatic index of $\gamma=1.25$, the ATMO2020++ and PH_3 -free ATMO2020++ models have slightly warmer atmospheres in the photospheres of W1 and [3.6] photometry as compared to models with the standard γ . However, our analysis suggests that such a γ , at least with this magnitude of modification, remains insufficient to match the observations (Figure 4). Other studies have also investigated

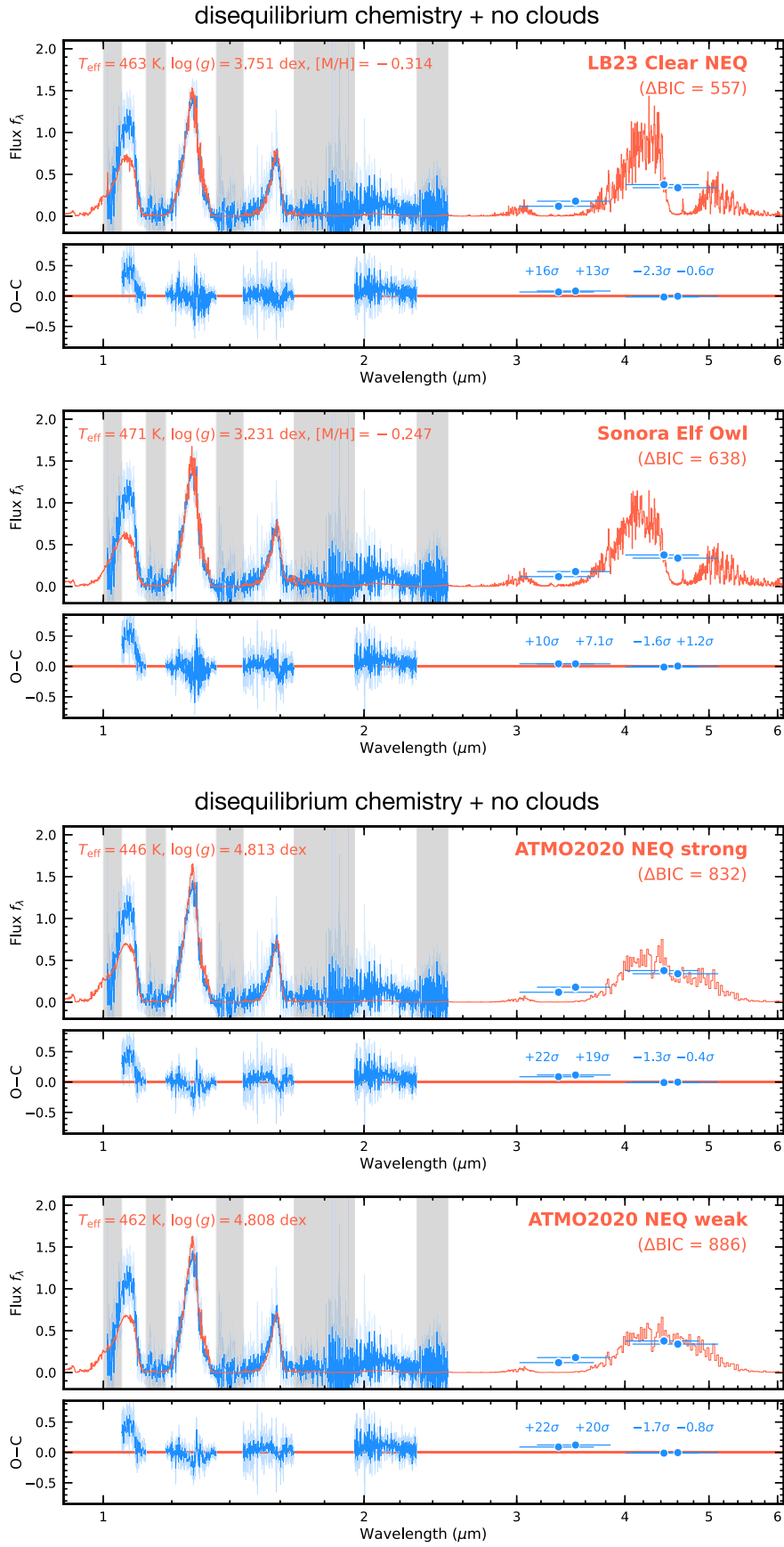


Figure 6. Forward-modeling results based on models that include disequilibrium chemistry and no clouds, with the same format as Figure 4.

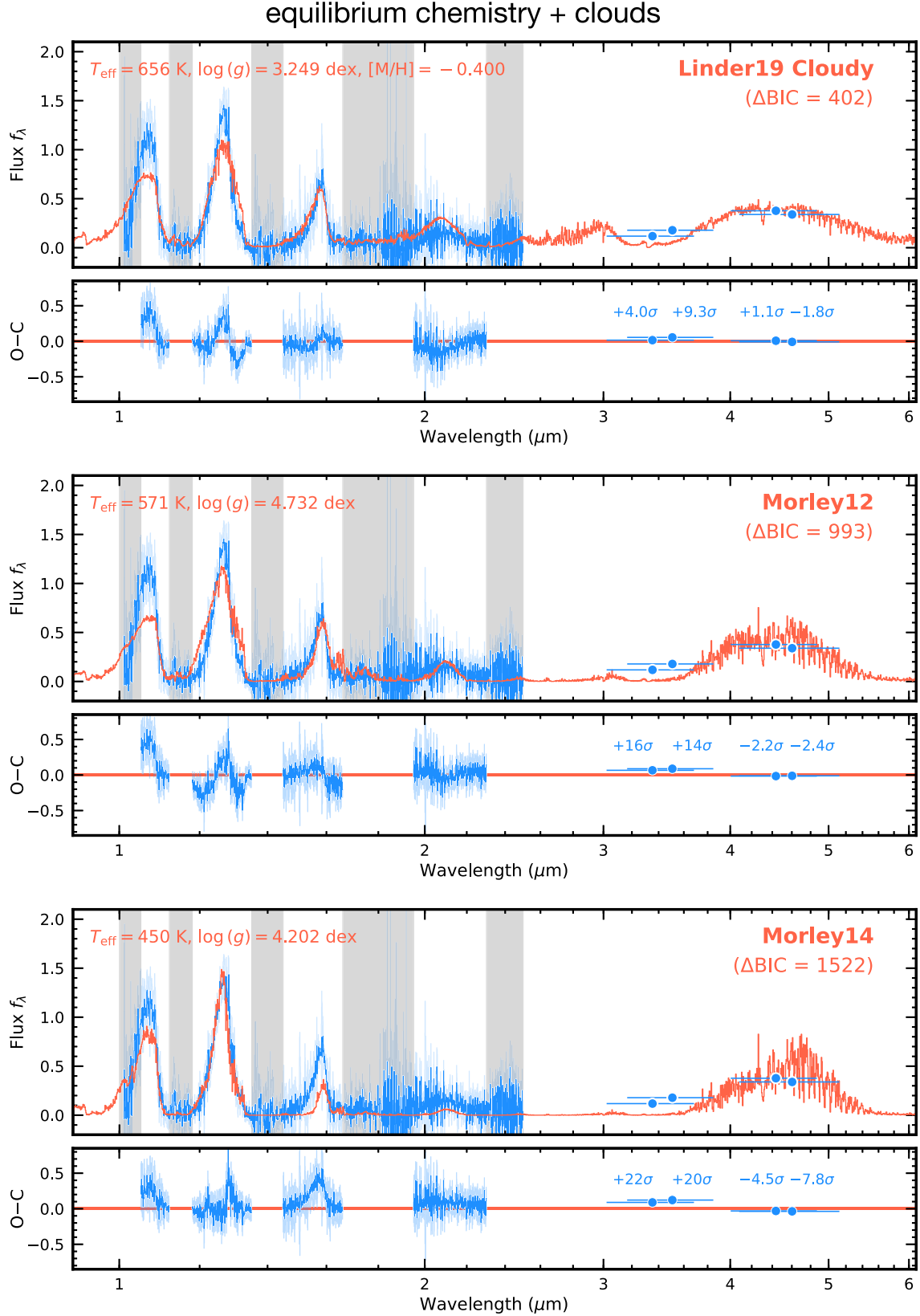


Figure 7. Forward-modeling results based on models that include equilibrium chemistry and clouds, with the same format as Figure 4.

atmospheric heating (e.g., S. Sorahana et al. 2014; B. Burningham et al. 2017), including C. V. Morley et al. (2018), who found no direct evidence for this effect in the atmosphere of WISE J085510.83–071442.5.

Interestingly, the Exo-REM models predict W1 and [3.6] values that are consistent with observations within 3σ . These models incorporate cloud opacities that are not included by most other grids, including ATMO2020++

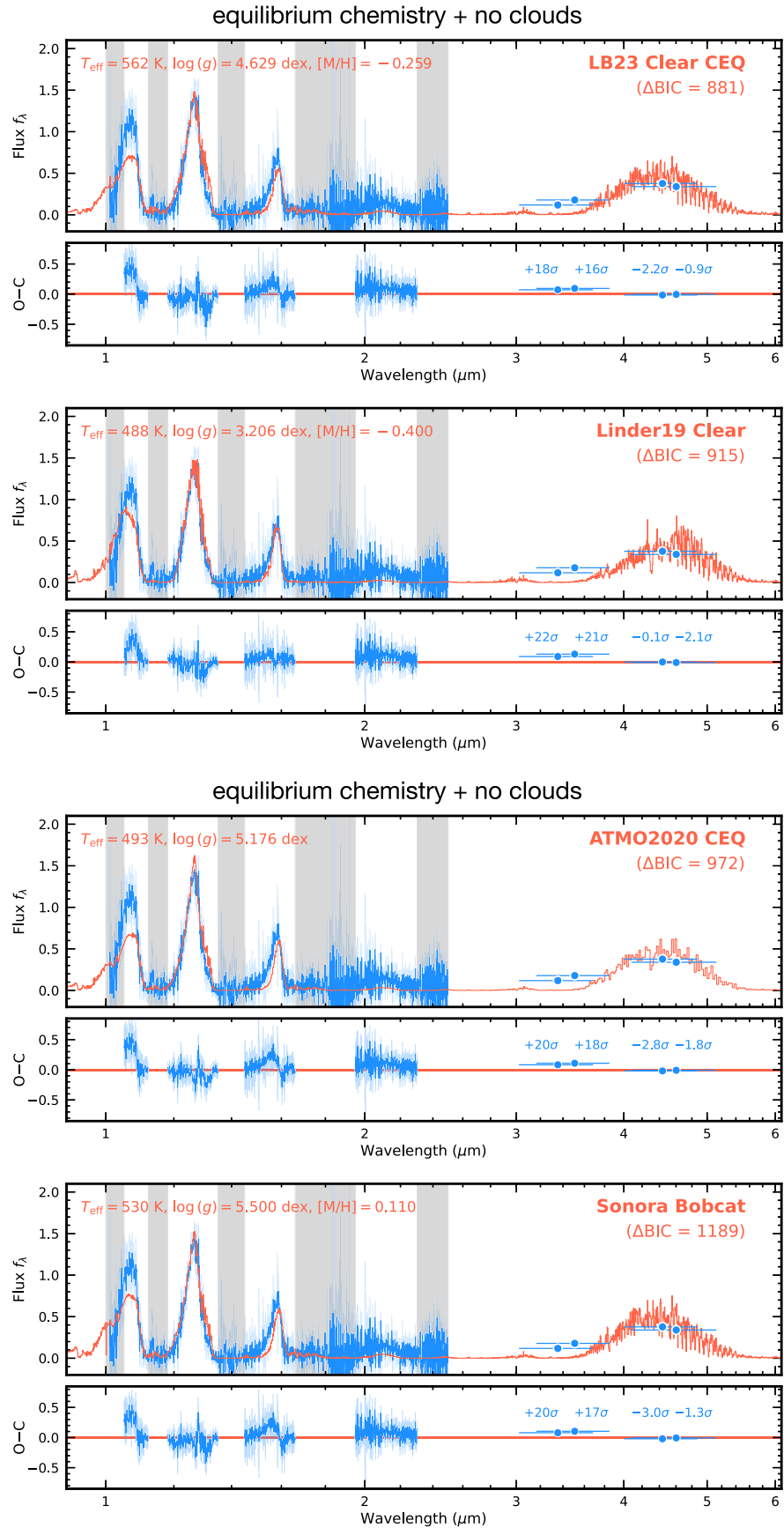


Figure 8. Forward-modeling results based on models that include equilibrium chemistry and no clouds, with the same format as Figure 4.

Table 1
Atmospheric Properties of COCONUTS-2b (Gemini/F2 Spectrum and W1/W2/[3.6]/[4.5] Photometry)

Atmospheric Model Grid	$\Delta \text{BIC}^{\text{a}}$	T_{eff} (K)	$\log(g)$ (dex)	[M/H] ^b (dex)	C/O ^b	$f_{\text{sed}}^{\text{b}}$	$\log(K_{zz})^{\text{b}}$ (cm ² s ⁻¹)	R (R_{Jup})	$\log(b)^{\text{c}}$ (erg s ⁻¹ cm ⁻² Å ⁻¹)	$\log(L_{\text{bol}}/L_{\odot})^{\text{c}}$ (dex)
disequilibrium chemistry + diabatic thermal structure + no clouds										
PH ₃ -free	0	545.5 ^{+3.3} _{-3.2}	4.174 ^{+0.024} _{-0.015}	-0.152 ^{+0.012} _{-0.010}	(0.55)	...	(6.65 ^{+0.03} _{-0.05})	0.878 ^{+0.014} _{-0.015}	-18.52 ^{+0.06} _{-0.07}	-6.179 ^{+0.005} _{-0.005}
ATMO2020++										
ATMO2020++	6	534.5 ^{+3.9} _{-3.8}	4.220 ^{+0.036} _{-0.039}	-0.209 ^{+0.025} _{-0.021}	(0.55)	...	(6.56 ^{+0.08} _{-0.07})	0.933 ^{+0.020} _{-0.020}	-18.54 ^{+0.06} _{-0.08}	-6.161 ^{+0.006} _{-0.006}
disequilibrium chemistry + clouds										
Exo-REM	111	449.9 ^{+0.4} _{-0.7}	3.348 ^{+0.004} _{-0.006}	-0.001 ^{+0.008} _{-0.009}	0.400 ^{+0.001} _{-0.000}	(microphys.)	(profile)	1.902 ^{+0.012} _{-0.011}	-18.34 ^{+0.04} _{-0.04}	-5.849 ^{+0.004} _{-0.004}
disequilibrium chemistry + no clouds										
LB23	557	463.2 ^{+1.0} _{-1.0}	3.758 ^{+0.012} _{-0.006}	-0.309 ^{+0.021} _{-0.021}	(0.537)	...	(profile)	1.149 ^{+0.009} _{-0.009}	-18.28 ^{+0.04} _{-0.04}	-6.225 ^{+0.004} _{-0.004}
Clear NEQ										
Sonora Elf Owl	638	472.7 ^{+4.6} _{-3.4}	3.235 ^{+0.007} _{-0.003}	-0.265 ^{+0.034} _{-0.040}	0.505 ^{+0.007} _{-0.004}	...	8.96 ^{+0.03} _{-0.06}	1.106 ^{+0.025} _{-0.031}	-18.33 ^{+0.04} _{-0.05}	-6.224 ^{+0.007} _{-0.008}
ATMO2020	832	445.6 ^{+2.6} _{-2.6}	4.810 ^{+0.035} _{-0.036}	(0)	(0.55)	...	(5.38 ^{+0.07} _{-0.07})	1.145 ^{+0.022} _{-0.022}	-18.38 ^{+0.04} _{-0.05}	-6.293 ^{+0.007} _{-0.007}
NEQ strong										
ATMO2020	886	461.7 ^{+2.4} _{-2.5}	4.808 ^{+0.038} _{-0.038}	(0)	(0.55)	...	(3.38 ^{+0.08} _{-0.08})	1.023 ^{+0.016} _{-0.016}	-18.40 ^{+0.05} _{-0.05}	-6.327 ^{+0.005} _{-0.005}
NEQ weak										
equilibrium chemistry + clouds										
Linder19	402	655.2 ^{+4.6} _{-5.6}	3.294 ^{+0.088} _{-0.083}	-0.398 ^{+0.004} _{-0.002}	(0.55)	0.93 ^{+0.12} _{-0.07}	...	0.586 ^{+0.006} _{-0.006}	-18.11 ^{+0.03} _{-0.04}	-6.226 ^{+0.011} _{-0.015}
Cloudy										
Morley12	993	570.3 ^{+4.9} _{-4.8}	4.720 ^{+0.054} _{-0.053}	(0)	(0.497)	4.97 ^{+0.02} _{-0.03}	...	0.621 ^{+0.010} _{-0.010}	-18.02 ^{+0.02} _{-0.02}	-6.406 ^{+0.005} _{-0.005}
Morley14 ^d	1522	449.9 ^{+0.1} _{-0.1}	4.205 ^{+0.036} _{-0.035}	(0)	(0.497)	(5)	...	1.024 ^{+0.005} _{-0.004}	-17.99 ^{+0.02} _{-0.02}	-6.360 ^{+0.004} _{-0.004}
equilibrium chemistry + no clouds										
LB23 Clear CEQ (M1) ^e	881	561.7 ^{+0.7} _{-0.9}	4.630 ^{+0.013} _{-0.015}	-0.261 ^{+0.012} _{-0.013}	(0.537)	0.630 ^{+0.004} _{-0.004}	-18.10 ^{+0.02} _{-0.02}	-6.408 ^{+0.004} _{-0.004}
LB23 Clear CEQ (M2) ^e	886	559.7 ^{+0.7} _{-0.7}	4.415 ^{+0.018} _{-0.012}	-0.311 ^{+0.012} _{-0.012}	(0.537)	0.633 ^{+0.004} _{-0.004}	-18.12 ^{+0.02} _{-0.02}	-6.411 ^{+0.004} _{-0.004}
Linder19 Clear	915	487.6 ^{+1.6} _{-1.6}	3.223 ^{+0.051} _{-0.051}	-0.394 ^{+0.010} _{-0.005}	(0.55)	0.863 ^{+0.008} _{-0.008}	-18.37 ^{+0.04} _{-0.05}	-6.379 ^{+0.004} _{-0.004}
ATMO2020 CEQ	972	493.0 ^{+2.0} _{-1.9}	5.178 ^{+0.042} _{-0.041}	(0)	(0.55)	0.834 ^{+0.008} _{-0.008}	-18.18 ^{+0.03} _{-0.03}	-6.387 ^{+0.004} _{-0.004}
Sonora Bobcat	1189	530.4 ^{+2.7} _{-2.7}	5.494 ^{+0.005} _{-0.010}	0.102 ^{+0.020} _{-0.021}	(0.458)	0.700 ^{+0.008} _{-0.008}	-18.19 ^{+0.03} _{-0.03}	-6.414 ^{+0.004} _{-0.004}

Notes.^a This column lists the BIC value of each model grid relative to that of the PH₃-free ATMO2020++ models.^b Values inside parentheses are fixed by the model grids. In particular, the log(K_{zz}) values of the ATMO2020, ATMO2020++, and PH₃-free ATMO2020++ modeling results are linearly interpolated from the inferred log(g) based on Figure 1 of Phillips et al. (2020).^c The bolometric luminosity is computed based on Equation (3) that accounts for the offsets between observed fluxes and the fitted models.^d The inferred T_{eff} based on Morley14 models is pinned at the maximum grid value at 450 K.^e The parameter posteriors inferred by the LB23 Clear CEQ grid exhibit two modes, with the corresponding results labeled as “M1” and “M2”.

and PH₃-free ATMO2020++. This suggests that cloud formation may be important in resolving the data-model offsets near 3.6 μm. Moreover, the improved data-model consistency of the Exo-REM models may also

stem from other factors, such as the opacities of key atmospheric absorbers (e.g., CH₄, collision-induced absorption by H₂) and the specific treatment of vertical mixing processes.

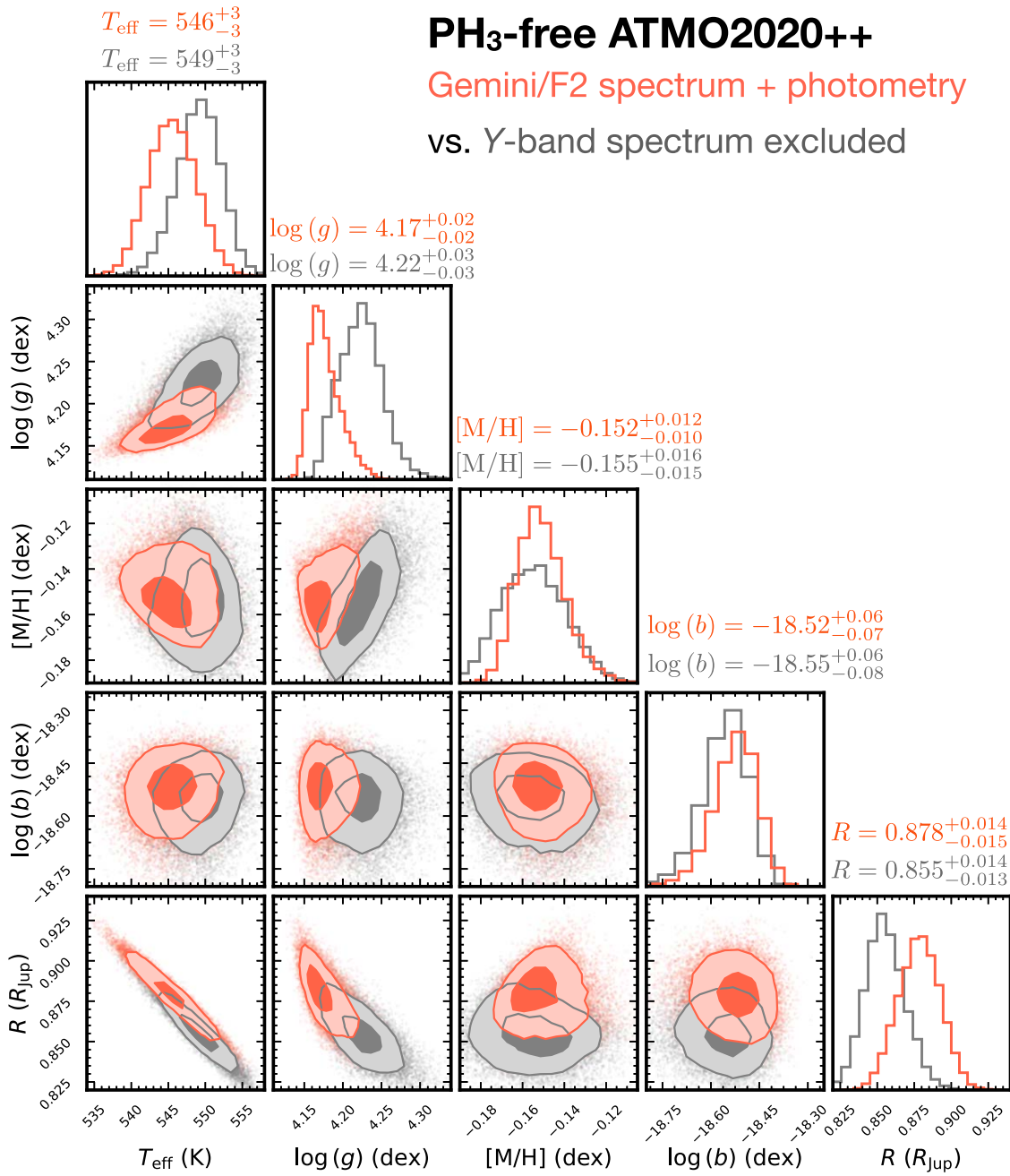


Figure 9. Posterior distributions of COCONUTS-2b’s spectroscopically inferred parameters using the PH_3 -free ATMO2020++ models. The results derived with the Y-band spectral fluxes included and excluded are shown in orange and gray, respectively. The 1σ and 2σ confidence intervals are highlighted.

5.2.3. Models with Equilibrium Chemistry and No Clouds: Underpredicted Fluxes in the H band

For model grids with equilibrium chemistry and no clouds, the predicted fluxes are too faint in the blue wing of the H band (Figure 8). This offset indicates the need for disequilibrium chemistry, which not only impacts the abundances of CH_4 and CO (Section 5.2.2) but also reduces the abundance of NH_3 (e.g., D. Saumon et al. 2006; K. J. Zahnle & M. S. Marley 2014). Incorporating disequilibrium chemistry into these models can lead to a depletion of NH_3 , which would enhance the model-predicted fluxes near $1.55 \mu\text{m}$ and help resolve the data-model discrepancies.

5.2.4. Models with Equilibrium Chemistry and Clouds: Offsets in the J band

For Linder19 Cloudy and Morley12 models that incorporate clouds into equilibrium chemistry, the predicted spectral shapes in the J band are too broad (Figure 7). These models also yield high T_{eff} values (570–655 K) that are 100–200 K hotter than predictions from most other atmospheric model grids (Table 1) and thermal evolution models (Section 5.4.2); their predicted radii (0.58 – $0.62 R_{\text{Jup}}$) are unphysically small compared to the evolution-based value of $1.11^{+0.03}_{-0.04} R_{\text{Jup}}$ (see Section 5.4.2). These chemical equilibrium cloudy models attempt to use clouds and hotter T_{eff} to

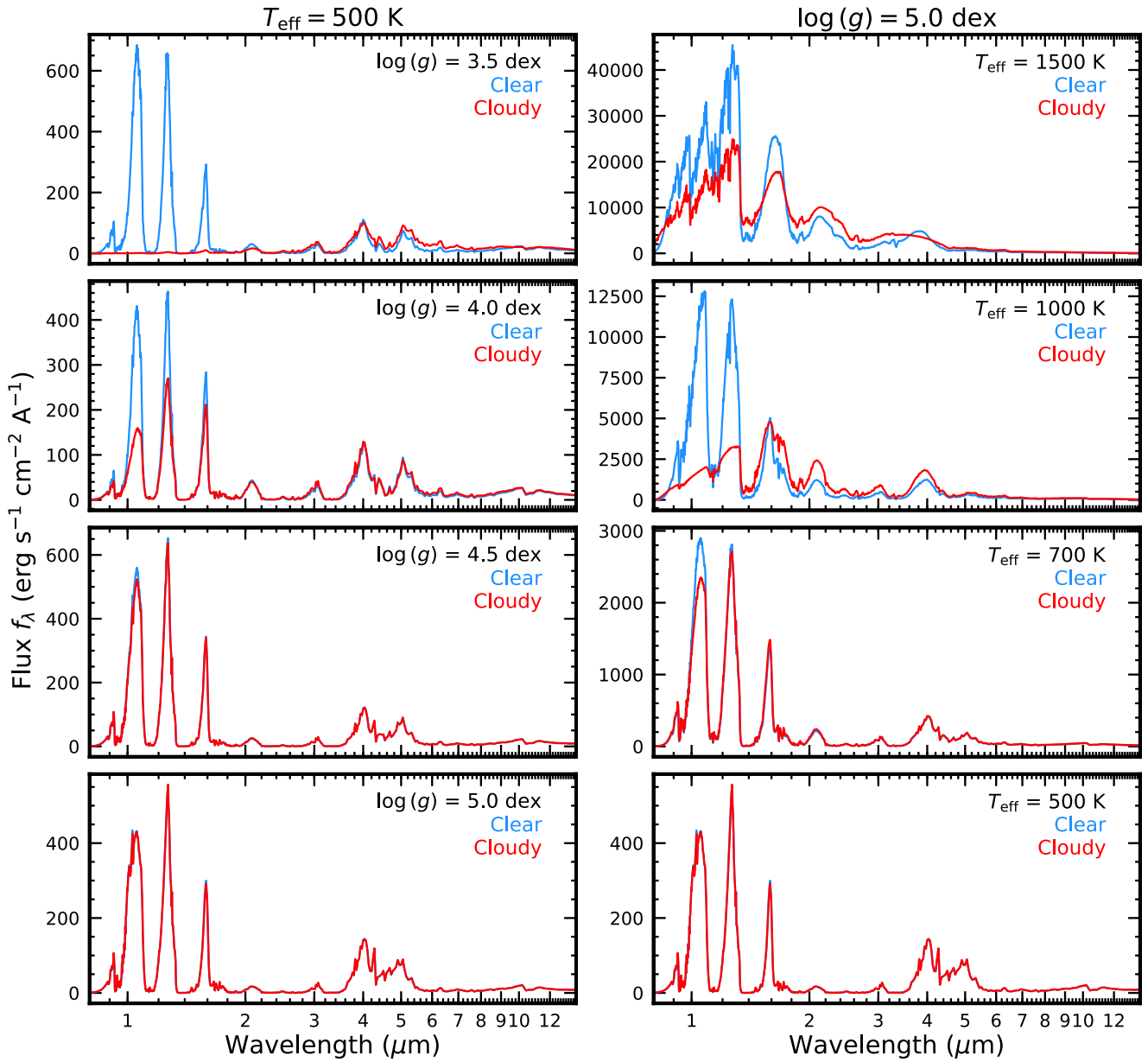


Figure 10. The Exo-REM $R \sim 500$ model spectra computed with cloud-free (blue) and cloudy (red) atmospheres. The left-hand column shows spectra with $T_{\text{eff}} = 500$ K and varying $\log(g)$; the integrated fluxes of these spectra over $0.34-250 \mu\text{m}$ are consistent within 0.004 dex. The right-hand column shows spectra with $\log(g) = 5.0$ dex and varying T_{eff} . All spectra correspond to $[\text{M}/\text{H}] = 0$ dex and $\text{C}/\text{O} = 0.4$, consistent with the inferred values for COCONUTS-2b based on Exo-REM (Table 1).

compensate for the lack of disequilibrium chemistry and avoid the H -band offsets discussed in the previous section. With T_{eff} around 600 K, sulfide clouds form at a few bars, attenuating the emergent fluxes in the Y and J bands and redistributing the fluxes toward longer wavelengths (e.g., K band and beyond), while not significantly altering fluxes in the H band (e.g., Figure 4 of C. V. Morley et al. 2012). Such a hotter atmosphere has a relatively lower chemical equilibrium abundance of NH_3 and CH_4 in the near-infrared photospheres, leading to a broader H -band shape (compared to predictions of chemical equilibrium models) that matches the observations. However, the hotter cloudy atmosphere also results in a broader J -band shape with a fainter peak flux, causing the data-model offsets in the J band.

These explanations are supported by the analysis results with Morley14 models. The inferred T_{eff} posterior is pinned at the maximum grid value of 450 K (Table 1), but this insufficiently

high temperature leaves the H -band data-model offsets unresolved (Figure 7).

5.2.5. Models with Disequilibrium Chemistry and No Clouds: Underpredicted Fluxes in the K band

For model grids with disequilibrium chemistry and no clouds, the predicted fluxes are too faint in the K band (Figure 6). This offset suggests the need for a modified adiabatic index or clouds. A slightly reduced adiabatic index (Section 5.1) can lead to hotter temperatures in the K -band photospheres, while clouds can redistribute the short-wavelength fluxes emergent from deep atmospheres to the K band and longer wavelengths (Section 5.2.4). Both effects can enhance the model-predicted fluxes in the K band, justifying why PH_3 -free ATMO2020++,

ATMO2020++, and Exo-REM are the preferred grids for interpreting the spectrophotometry of COCONUTS-2b.

5.3. Impact of the Input Spectrophotometry

We repeat the forward-modeling analysis with variations in COCONUTS-2b's spectrophotometry to assess their impacts on our results.

In the first experiment, we perform the analysis with the Y -band spectrum fully masked, focusing on fitting the spectrum over 1.18–1.35 μm , 1.45–1.66 μm , and 1.95–2.30 μm , along with $W1$, $W2$, [3.6], and [4.5] photometry. This approach is motivated by the persistent Y -band data-model offsets among all model grids in our analysis (Section 5.2.1). The PH_3 -free ATMO2020++, ATMO2020++ and Exo-REM models remain the most preferred grids for interpreting the spectrophotometry of COCONUTS-2b. Notably, several model grids—including ATMO2020++, Exo-REM, ATMO2020 NEQ strong, ATMO2020 NEQ weak, and LB23 Clear CEQ—exhibit bimodal parameter posteriors (Table 2). In contrast, when the Y -band spectrum is included in spectral fits, only the LB23 Clear CEQ model grid yields bimodal posteriors.

For the three preferred model grids, we also assess the changes in the inferred parameters between fits with and without the Y -band spectrum. For PH_3 -free ATMO2020++ and Exo-REM, most physical parameters remain consistent within 1.5σ . The only significant deviation is found in the [M/H] predicted by Exo-REM, where including the Y -band spectrum leads to a [M/H] value that is 10σ higher than one of the modes inferred without Y band. Additionally, parameter shifts in ATMO2020++ become more significant, ranging from 4σ – 12σ , with absolute differences of 20–30 K in T_{eff} , 0.4–0.5 dex in $\log(g)$, 0.05–0.23 dex in [M/H], and 0.08–0.10 R_{Jup} in radius.

In the second experiment, we keep the same spectral wavelength ranges as in the main analysis (Section 4) but additionally include the $W3$ photometry. No significant changes are found in the results. The inferred parameters of these two experiments are summarized in Tables 2 and 3. Figures presenting data-model comparisons are presented in Appendix C.

5.4. A Recommended Set of Physical Properties for COCONUTS-2b

The forward-modeling analyses provide valuable insights into the atmospheric processes of COCONUTS-2b, yet the resulting physical properties of different model grids differ noticeably. These spectroscopically inferred physical parameters may carry systematic errors (e.g., Z. Zhang et al. 2021b, 2021c; S. A. Hurt et al. 2024), stemming from uncertainties in opacity databases and assumptions about exoplanet atmospheres. Thermal evolution models offer a complementary perspective on the fundamental properties of self-luminous exoplanets, brown dwarfs, and stars because these models are less affected by some of these systematic effects (e.g., Section 5.1 of Z. Zhang et al. 2023a and references therein).

In this section, we summarize the physical properties of COCONUTS-2b by combining the results of our forward-modeling analysis with predictions from various thermal evolution models. We focus on bolometric luminosity (Section 5.4.1), effective temperature, surface gravity, radius, and mass (Section 5.4.2).

5.4.1. Bolometric Luminosity

Table 1 lists the inferred bolometric luminosities based on each model grid. These L_{bol} values are computed with data-model discrepancies already incorporated (Equation (3)). Therefore, the variations in L_{bol} among model grids primarily reflect the different assumptions of each model rather than the quality of the spectral fits.

We adopt the bolometric luminosity value from the most preferred grid, which is $\log(L_{\text{bol}}/L_{\odot}) = -6.18$ dex, along with a 0.5 dex wide range of $[-6.43, -5.93]$ dex to encompass the scatter of predicted values across different model grids.²⁶ The bolometric luminosity of COCONUTS-2b will be more precisely constrained by the upcoming JWST NIRSPEC and MIRI observations.

5.4.2. Effective Temperature, Surface Gravity, Radius, and Mass

We derive the physical properties of COCONUTS-2b using several thermal evolution models (Table 4), including the hot-start ATMO2020 models (M. W. Phillips et al. 2020) and both the hot-start and cold-start Sonora Bobcat models (M. S. Marley et al. 2021b). We assume uniform distributions for $\log(L_{\text{bol}}/L_{\odot})$ and age, ranging from -6.43 to -5.93 dex (Section 5.4.1) and from 150 to 800 Myr (Z. Zhang et al. 2021a), respectively. The evolution models are interpolated on a linear scale for $\log(g)$ and logarithmic scales for T_{eff} , L_{bol} , age, R , and M .

The inferred parameters are summarized in Table 4. Given the consistency of predictions across different evolution models, we concatenate the chains of a given parameter derived from all models and adopt the median values and confidence intervals. Based on all these evolution models, COCONUTS-2b has $T_{\text{eff}} = 483^{+44}_{-53}$ K, $\log(g) = 4.19^{+0.18}_{-0.13}$ dex, $R = 1.11^{+0.03}_{-0.04} R_{\text{Jup}}$, and $M = 8 \pm 2 M_{\text{Jup}}$. Considering the mass of COCONUTS-2A ($0.37 \pm 0.02 M_{\odot}$; Z. Zhang et al. 2021a), the companion-to-host mass ratio of this system is 0.021 ± 0.005 .

Figure 11 compares these evolution-based parameters with those inferred from atmospheric models through spectral fitting (Section 4). For the three preferred model grids, PH_3 -free ATMO2020++, ATMO2020++, and Exo-REM, their inferred effective temperatures align well with predictions from the thermal evolution models. The $\log(g)$ and M values inferred by PH_3 -free ATMO2020++ and ATMO2020++ also match the evolution-based parameters, while Exo-REM predicts lower values. However, all three model grids predict different radii with evolution-based values, with Exo-REM showing significantly larger inconsistencies than PH_3 -free ATMO2020++ and ATMO2020++. Beyond these three model grids, several other grids predict unphysically small radii, near $0.6 R_{\text{Jup}}$ (Table 1), which contradict the fundamental mass-radius relationship for brown dwarfs (A. Burrows et al. 1989; D. Saumon et al. 1996; M. S. Marley et al. 2021b). These discrepancies between atmospheric and evolution model predictions have been reported for other gas-giant exoplanets and brown dwarfs (e.g., E. C. Gonzales et al. 2020; Z. Zhang et al. 2020, 2021b, 2021c; J. A. Zalesky et al. 2022; C. E. Hood et al. 2023; S. A. Hurt et al. 2024; M. W. Phillips et al. 2024). These differences may arise from uncertainties in the opacities

²⁶ Z. Zhang et al. (2021a) estimated $\log(L_{\text{bol}}/L_{\odot}) = -6.384 \pm 0.028$ dex by combining J_{MKO} , K_{MKO} , [3.6], and [4.5] broadband photometry. They used the “super-magnitude” bolometric correction, which is based on the Sonora Bobcat and ATMO2020 models (see W. M. J. Best et al. 2024b). Our computed bolometric luminosities from these two model grids, as shown in Tables 1–3, yield consistent values with Z. Zhang et al. (2021a).

Table 2
Atmospheric Properties of COCONUTS-2b (*Y*-band Spectrum Excluded)

Atmospheric Model Grid	$\Delta\text{BIC}^{\text{a}}$	T_{eff} (K)	$\log(g)$ (dex)	[M/H] ^b (dex)	C/O ^c	$f_{\text{sed}}^{\text{b}}$	$\log(K_{zz})^{\text{b}}$ (cm ² s ⁻¹)	R (R_{Jup})	$\log(b)^{\text{b}}$ (erg s ⁻¹ cm ⁻² Å ⁻¹)	$\log(L_{\text{bol}}/L_{\odot})^{\text{c}}$ (dex)
disequilibrium chemistry + diabatic thermal structure + no clouds										
ATMO2020++ (M1) ^d	-34	563.1 ^{+2.8} _{-2.0}	4.611 ^{+0.015} _{-0.014}	-0.105 ^{+0.012} _{-0.012}	(0.55)	...	(5.78 ^{+0.03} _{-0.03})	0.795 ^{+0.011} _{-0.011}	-18.60 ^{+0.07} _{-0.09}	-6.215 ^{+0.005} _{-0.005}
ATMO2020++ (M2) ^d	-33	555.0 ^{+2.4} _{-2.5}	4.682 ^{+0.018} _{-0.014}	0.024 ^{+0.012} _{-0.012}	(0.55)	...	(5.64 ^{+0.03} _{-0.04})	0.826 ^{+0.011} _{-0.011}	-18.68 ^{+0.09} _{-0.14}	-6.207 ^{+0.005} _{-0.005}
PH ₃ -free ATMO2020++	0	549.3 ^{+3.8} _{-3.1}	4.223 ^{+0.027} _{-0.028}	-0.155 ^{+0.016} _{-0.015}	(0.55)	...	(6.55 ^{+0.06} _{-0.05})	0.855 ^{+0.014} _{-0.013}	-18.55 ^{+0.06} _{-0.08}	-6.194 ^{+0.005} _{-0.006}
disequilibrium chemistry + clouds										
Exo-REM (M1) ^d	209	452.9 ^{+1.8} _{-1.9}	3.332 ^{+0.011} _{-0.010}	-0.132 ^{+0.010} _{-0.009}	0.435 ^{+0.002} _{-0.003}	(microphys.)	(profile)	1.887 ^{+0.025} _{-0.024}	-18.38 ^{+0.04} _{-0.05}	-5.845 ^{+0.005} _{-0.006}
Exo-REM (M2) ^d	214	450.0 ^{+0.7} _{-0.9}	3.340 ^{+0.005} _{-0.008}	-0.011 ^{+0.010} _{-0.018}	0.400 ^{+0.001} _{-0.000}	(microphys.)	(profile)	1.904 ^{+0.014} _{-0.012}	-18.41 ^{+0.04} _{-0.05}	-5.848 ^{+0.005} _{-0.005}
disequilibrium chemistry + no clouds										
Sonora Elf Owl	605	469.2 ^{+2.7} _{-2.7}	3.243 ^{+0.021} _{-0.009}	-0.276 ^{+0.027} _{-0.028}	0.503 ^{+0.005} _{-0.003}	...	8.98 ^{+0.01} _{-0.03}	1.116 ^{+0.021} _{-0.020}	-18.40 ^{+0.05} _{-0.05}	-6.233 ^{+0.006} _{-0.007}
LB23 Clear NEQ	638	464.7 ^{+1.1} _{-1.2}	3.791 ^{+0.013} _{-0.020}	-0.320 ^{+0.021} _{-0.022}	(0.537)	...	(profile)	1.131 ^{+0.010} _{-0.010}	-18.31 ^{+0.04} _{-0.04}	-6.237 ^{+0.004} _{-0.004}
ATMO2020 NEQ strong (M1) ^d	903	465.7 ^{+2.7} _{-2.7}	5.130 ^{+0.033} _{-0.033}	(0)	(0.55)	...	(4.74 ^{+0.07} _{-0.07})	1.000 ^{+0.014} _{-0.014}	-18.32 ^{+0.04} _{-0.04}	-6.337 ^{+0.004} _{-0.004}
ATMO2020 NEQ strong (M2) ^d	908	449.1 ^{+2.3} _{-2.3}	4.896 ^{+0.031} _{-0.032}	(0)	(0.55)	...	(5.21 ^{+0.06} _{-0.06})	1.101 ^{+0.020} _{-0.017}	-18.40 ^{+0.04} _{-0.05}	-6.317 ^{+0.007} _{-0.006}
ATMO2020 NEQ weak (M1) ^d	942	476.4 ^{+2.1} _{-2.2}	5.139 ^{+0.033} _{-0.035}	(0)	(0.55)	...	(2.72 ^{+0.07} _{-0.07})	0.933 ^{+0.011} _{-0.011}	-18.32 ^{+0.04} _{-0.04}	-6.357 ^{+0.004} _{-0.004}
ATMO2020 NEQ weak (M2) ^d	951	463.8 ^{+2.4} _{-2.4}	4.900 ^{+0.039} _{-0.039}	(0)	(0.55)	...	(3.20 ^{+0.08} _{-0.08})	0.999 ^{+0.015} _{-0.016}	-18.41 ^{+0.05} _{-0.05}	-6.345 ^{+0.004} _{-0.005}
equilibrium chemistry + clouds										
Linder19 Cloudy	504	640.4 ^{+3.2} _{-3.7}	3.597 ^{+0.040} _{-0.042}	-0.395 ^{+0.007} _{-0.003}	(0.55)	0.90 ^{+0.06} _{-0.04}	...	0.593 ^{+0.005} _{-0.005}	-18.17 ^{+0.03} _{-0.03}	-6.253 ^{+0.009} _{-0.011}
Morley12	1044	580.9 ^{+4.7} _{-4.6}	4.944 ^{+0.040} _{-0.054}	(0)	(0.497)	4.93 ^{+0.05} _{-0.10}	...	0.599 ^{+0.009} _{-0.009}	-18.01 ^{+0.02} _{-0.02}	-6.410 ^{+0.005} _{-0.004}
Morley14 ^e	1687	449.9 ^{+0.1} _{-0.1}	4.394 ^{+0.048} _{-0.041}	(0)	(0.497)	(5)	...	1.012 ^{+0.005} _{-0.004}	-17.99 ^{+0.02} _{-0.02}	-6.372 ^{+0.004} _{-0.004}
equilibrium chemistry + no clouds										
LB23 Clear CEQ (M1) ^d	987	550.1 ^{+1.3} _{-1.1}	4.995 ^{+0.004} _{-0.009}	-0.167 ^{+0.014} _{-0.015}	(0.537)	0.650 ^{+0.004} _{-0.004}	-18.08 ^{+0.02} _{-0.02}	-6.420 ^{+0.004} _{-0.004}
LB23 Clear CEQ (M2) ^d	990	559.1 ^{+1.4} _{-2.6}	4.667 ^{+0.028} _{-0.019}	-0.279 ^{+0.020} _{-0.016}	(0.537)	0.634 ^{+0.006} _{-0.006}	-18.10 ^{+0.02} _{-0.02}	-6.415 ^{+0.004} _{-0.005}
ATMO2020 CEQ	1047	495.6 ^{+2.0} _{-2.0}	5.351 ^{+0.046} _{-0.045}	(0)	(0.55)	0.822 ^{+0.009} _{-0.009}	-18.15 ^{+0.03} _{-0.03}	-6.396 ^{+0.004} _{-0.004}
Linder19 Clear	1051	483.0 ^{+2.1} _{-2.8}	3.539 ^{+0.064} _{-0.081}	-0.389 ^{+0.019} _{-0.008}	(0.55)	0.876 ^{+0.013} _{-0.014}	-18.35 ^{+0.04} _{-0.05}	-6.386 ^{+0.004} _{-0.004}
Sonora Bobcat	1340	547.3 ^{+3.6} _{-3.5}	5.322 ^{+0.061} _{-0.062}	-0.123 ^{+0.027} _{-0.027}	(0.458)	0.665 ^{+0.008} _{-0.008}	-18.11 ^{+0.03} _{-0.03}	-6.410 ^{+0.005} _{-0.005}

Notes.

^a This column lists the BIC value of each model grid relative to that of the PH₃-free ATMO2020++ models.

^b Values inside parentheses are fixed by the model grids. In particular, the log(K_{zz}) values of the ATMO2020, ATMO2020++, and PH₃-free ATMO2020++ modeling results are linearly interpolated from the inferred log(g) based on Figure 1 of Phillips et al. (2021).

^c The bolometric luminosity is computed based on Equation (3) that accounts for the offsets between observed fluxes and the fitted models.

^d The parameter posteriors inferred by these model grids exhibit two modes, with the corresponding results labeled as “M1” and “M2”.

^e The inferred T_{eff} based on Morley14 models is pinned at the maximum grid value at 450 K.

Table 3
Atmospheric Properties of COCONUTS-2b (W3 Photometry Included)

Atmospheric Model Grid ^a	$\Delta \text{BIC}^{\text{b}}$	T_{eff} (K)	$\log(g)$ (dex)	[M/H] ^c (dex)	C/O ^c	$f_{\text{sed}}^{\text{c}}$	$\log(K_{zz})^{\text{c}}$ ($\text{cm}^2 \text{s}^{-1}$)	R (R_{Jup})	$\log(b)^{\text{d}}$ ($\text{erg s}^{-1} \text{cm}^{-2} \text{\AA}^{-1}$)	$\log(L_{\text{bol}}/L_{\odot})^{\text{d}}$ (dex)
disequilibrium chemistry + diabatic thermal structure + no clouds										
PH ₃ -free ATMO2020	0	544.6 ^{+3.3} _{-3.2}	4.170 ^{+0.022} _{-0.014}	-0.151 ^{+0.012} _{-0.010}	(0.55)	...	(6.66 ^{+0.03} _{-0.04})	0.883 ^{+0.014} _{-0.015}	-18.52 ^{+0.06} _{-0.07}	-6.177 ^{+0.005} _{-0.005}
++ ATMO2020++	4	533.2 ^{+3.9} _{-3.9}	4.212 ^{+0.034} _{-0.041}	-0.208 ^{+0.024} _{-0.021}	(0.55)	...	(6.58 ^{+0.08} _{-0.07})	0.940 ^{+0.020} _{-0.020}	-18.54 ^{+0.06} _{-0.08}	-6.159 ^{+0.007} _{-0.006}
disequilibrium chemistry + clouds										
Exo-REM	105	449.9 ^{+0.4} _{-0.6}	3.349 ^{+0.004} _{-0.006}	-0.001 ^{+0.008} _{-0.009}	0.400 ^{+0.000} _{-0.000}	(microphys.)	(profile)	1.899 ^{+0.012} _{-0.011}	-18.34 ^{+0.04} _{-0.05}	-5.850 ^{+0.004} _{-0.004}
disequilibrium chemistry + no clouds										
LB23 Clear NEQ ATMO2020 NEQ strong ATMO2020 NEQ weak	562 842 899	463.1 ^{+1.0} _{-1.0} 444.9 ^{+2.6} _{-2.6} 461.1 ^{+2.4} _{-2.5}	3.759 ^{+0.012} _{-0.006} 4.799 ^{+0.036} _{-0.036} 4.799 ^{+0.038} _{-0.039}	-0.304 ^{+0.021} _{-0.021} (0) (0)	(0.537) (0.55) (0.55)	...	(profile)	1.151 ^{+0.009} _{-0.009} 1.152 ^{+0.022} _{-0.022} (3.40 ^{+0.08} _{-0.08})	-18.28 ^{+0.04} _{-0.04} -18.38 ^{+0.04} _{-0.05} 1.027 ^{+0.017} _{-0.016}	-6.225 ^{+0.004} _{-0.004} -6.291 ^{+0.007} _{-0.007} -18.41 ^{+0.05} _{-0.05}
equilibrium chemistry + clouds										
Linder19 Cloudy Morley12 Morley14 ^e	390 1015 1538	676.1 ^{+2.8} _{-3.2} 570.0 ^{+4.8} _{-4.9} 449.9 ^{+0.1} _{-0.1}	3.251 ^{+0.027} _{-0.036} 4.718 ^{+0.053} _{-0.055} 4.204 ^{+0.034} _{-0.035}	-0.396 ^{+0.006} _{-0.003} (0) (0)	(0.55) (0.497) (0.497)	0.78 ^{+0.03} 4.97 ^{+0.02} (5)	...	0.575 ^{+0.005} _{-0.005} 0.622 ^{+0.010} _{-0.010} 1.024 ^{+0.004} _{-0.004}	-18.08 ^{+0.02} _{-0.02} -18.02 ^{+0.02} _{-0.02} -17.99 ^{+0.02} _{-0.02}	-6.186 ^{+0.006} _{-0.006} -6.405 ^{+0.005} _{-0.005} -6.360 ^{+0.004} _{-0.004}
equilibrium chemistry + no clouds										
LB23 Clear CEQ (M1) ^f LB23 Clear CEQ (M2) ^f Linder19 Clear ATMO2020 CEQ Sonora Bobcat	906 910 935 993 1298	561.7 ^{+0.7} _{-0.8} 559.6 ^{+0.7} _{-0.7} 487.5 ^{+1.6} _{-1.6} 493.0 ^{+2.0} _{-1.9} 530.3 ^{+2.6} _{-2.7}	4.630 ^{+0.013} _{-0.016} 4.415 ^{+0.019} _{-0.012} 3.218 ^{+0.052} _{-0.050} 5.179 ^{+0.042} _{-0.041} 5.493 ^{+0.005} _{-0.010}	-0.262 ^{+0.012} _{-0.012} -0.312 ^{+0.012} _{-0.013} -0.394 ^{+0.010} _{-0.005} (0) 0.102 ^{+0.020} _{-0.021}	(0.537) (0.537) (0.55) (0.55) (0.458)	0.631 ^{+0.004} _{-0.004} 0.633 ^{+0.004} _{-0.004} 0.864 ^{+0.008} _{-0.009} 0.835 ^{+0.008} _{-0.008} 0.701 ^{+0.008} _{-0.008}	-18.10 ^{+0.02} _{-0.02} -18.12 ^{+0.03} _{-0.02} -18.37 ^{+0.04} _{-0.05} -18.18 ^{+0.03} _{-0.03} -18.19 ^{+0.03} _{-0.03}	-6.408 ^{+0.004} _{-0.004} -6.411 ^{+0.004} _{-0.004} -6.378 ^{+0.004} _{-0.004} -6.387 ^{+0.004} _{-0.004} -6.414 ^{+0.004} _{-0.004}

Notes.

^a The Sonora Elf Owl models are not used because the synthetic spectra (with a wavelength cutoff at 15 μm) do not cover the full wavelength of the W3 filter response.

^b This column lists the BIC value of each model grid relative to that of the PH₃-free ATMO2020++ models.

^c Values inside parentheses are fixed by the model grids. In particular, the $\log(K_{zz})$ values of the ATMO2020, ATMO2020++, and PH₃-free ATMO2020++ modeling results are linearly interpolated from the inferred $\log(g)$ based on Figure 1 of Phillips et al. (2021).

^d The bolometric luminosity is computed based on Equation (3) that accounts for the offsets between observed fluxes and the fitted models.

^e The inferred T_{eff} based on Morley14 models is pinned at the maximum grid value at 450 K.

^f The parameter posteriors inferred by the LB23 Clear CEQ grid exhibit two modes, with the corresponding results labeled as “M1” and “M2”.

adopted by the atmospheric models, assumptions within atmospheric and evolution models, or unknown factors such as the binarity or age uncertainties of the objects (see also Section 5.1 of Z. Zhang et al. 2023a).

Additionally, the uncertainties in parameters inferred from atmospheric models are significantly smaller than those derived from evolution models. Similar trends of small statistical uncertainties from atmospheric models have been also

Table 4
Evolution-based Properties of COCONUTS-2b Based on L_{bol} and Age

Evolution Models	T_{eff}		R		$\log g$		M	
	Median $\pm 1\sigma$ (K)	3 σ C. I. (K)	Median $\pm 1\sigma$ (R_{Jup})	3 σ C. I. (R_{Jup})	Median $\pm 1\sigma$ (dex)	3 σ C. I. (dex)	Median $\pm 1\sigma$ (M_{Jup})	3 σ C. I. (M_{Jup})
hot-start ATMO2020	490^{+47}_{-52}	(416, 577)	$1.09^{+0.03}_{-0.04}$	(1.05, 1.16)	$4.21^{+0.18}_{-0.14}$	(3.8, 4.5)	8^{+2}_{-2}	(3, 12)
hot-start Sonora Bobcat [M/H] = +0.5	488^{+47}_{-52}	(413, 575)	$1.10^{+0.03}_{-0.04}$	(1.05, 1.17)	$4.20^{+0.19}_{-0.14}$	(3.8, 4.4)	8^{+2}_{-2}	(3, 12)
hot-start Sonora Bobcat [M/H] = 0	485^{+47}_{-52}	(411, 570)	$1.12^{+0.03}_{-0.04}$	(1.07, 1.19)	$4.18^{+0.18}_{-0.14}$	(3.8, 4.4)	8^{+2}_{-2}	(3, 12)
hot-start Sonora Bobcat [M/H] = -0.5	484^{+46}_{-51}	(410, 569)	$1.12^{+0.03}_{-0.04}$	(1.07, 1.19)	$4.16^{+0.19}_{-0.13}$	(3.7, 4.4)	7^{+2}_{-2}	(3, 11)
cold-start Sonora Bobcat [M/H] = 0	466^{+33}_{-47}	(411, 561)	$1.12^{+0.03}_{-0.04}$	(1.07, 1.18)	$4.17^{+0.17}_{-0.10}$	(3.8, 4.3)	7^{+2}_{-2}	(3, 10)
Adopted ^a	483^{+44}_{-53}	(411, 575)	$1.11^{+0.03}_{-0.04}$	(1.05, 1.19)	$4.19^{+0.18}_{-0.13}$	(3.7, 4.4)	8^{+2}_{-2}	(3, 12)

Note.

^a The adopted parameters are inferred from the concatenated chains of all the evolution models (Section 5.4.2).

observed in previous forward-modeling studies (e.g., S. K. Leggett et al. 2007; E. L. Rice et al. 2010; Z. Zhang et al. 2020; S. A. Hurt et al. 2024; S. Petrus et al. 2024; M. W. Phillips et al. 2024). A more sophisticated likelihood function that accounts for model interpolation uncertainties and correlations in data-model residuals across adjacent wavelengths may provide more realistic parameter uncertainties (e.g., I. Czekala et al. 2015; Z. Zhang et al. 2021b, 2021c).

5.5. The Subsolar/Near-solar [M/H] and C/O in the Atmosphere of COCONUTS-2b

Most atmospheric models predict a subsolar metallicity for COCONUTS-2b, regardless of variations in the input spectrophotometry used for spectral fits (Figure 11). However, exceptions exist where the inferred metallicities are closer to the solar value (Tables 1–3). Specifically, when Y-band fluxes are included in the spectral fits, the Exo-REM grid yields [M/H] = $-0.001^{+0.008}_{-0.009}$ dex; also, the least preferred grid, Sonora Bobcat, gives [M/H] = $0.102^{+0.020}_{-0.021}$ dex. When the Y-band fluxes are excluded, the ATMO2020++ and Exo-REM grids show bimodal posterior distributions. In both grids, the mode with higher log-likelihood values suggests a subsolar metallicity, while the other mode indicates a near-solar value (Table 2). Furthermore, the only two model grids with nonsolar C/O axes, Exo-REM and Sonora Elf Owl, suggest C/O of 0.4–0.5. These values are lower than or comparable with the solar C/O range of 0.45–0.55 as reported by, e.g., K. Lodders (2003), M. Asplund et al. (2006, 2009), K. Lodders (2010b), and E. Caffau et al. (2011). These metallicity and C/O estimates for COCONUTS-2b should be validated with upcoming JWST observations, which will cover a broader wavelength range. As shown by S. Petrus et al. (2024), the spectroscopically inferred [M/H] and C/O ratios for a L-type brown dwarf can be sensitive to the spectral wavelength range used in the fit.

In summary, our analysis indicates that COCONUTS-2b's atmosphere has subsolar or near-solar [M/H] and C/O. Similar findings were also reported for WASP-77 Ab (M. R. Line et al. 2021; P. C. August et al. 2023). A subsolar atmospheric [M/H] suggests that COCONUTS-2b was not influenced by core erosion or planetesimal bombardment processes that can lead to metal enrichment in the atmospheres (e.g., Y. Alibert et al. 2005; N. Miller & J. J. Fortney 2011; N. Madhusudhan 2019; D. Thorngren & J. J. Fortney 2019; A. D. Schneider & B. Bitsch 2021; Z. Zhang et al. 2023a; E. M.-R. Kempton & H. A. Knutson 2024). The subsolar/near-solar C/O may be

explained if COCONUTS-2b initially assembled its atmosphere at very close orbital separations from its parent star, accreting oxygen-rich and carbon-depleted gas from within ice lines (e.g., M. R. Line et al. 2021; P. C. August et al. 2023). This process might have been followed by outward migration after disk dissipation (driven by, e.g., planet–planet interactions and stellar fly-bys; F. Marocco et al. 2024), bringing COCONUTS-2b to its current wide orbit.

Additionally, our most preferred grid, PH₃-free ATMO-2020++, estimates a metallicity of [M/H] = $-0.152^{+0.012}_{-0.010}$ dex for COCONUTS-2b, which is a factor of $0.71^{+0.14}_{-0.12}$ relative to the metallicity of its parent star, COCONUTS-2A ([M/H]_A = 0.00 ± 0.08 dex; S. Hojjatpanah et al. 2019). This 2 σ difference in [M/H] between COCONUTS-2b and 2A lowers the likelihood of an in situ, stellar-binary-like formation scenario. However, our third-preferred grid, Exo-REM, suggests that COCONUTS-2b and 2A have consistent atmospheric metallicities, which supports a binary-like formation pathway.

6. Summary

We have studied COCONUTS-2b's atmospheric properties based on our newly observed 1.0–2.5 μm spectroscopy from Gemini/FLAMINGOS-2. The main findings are summarized below.

1. COCONUTS-2b straddles the T/Y transition with a spectral type of $T9.5 \pm 0.5$, as determined by comparing our Gemini/F2 spectrum to the near-infrared spectra of T0–Y1 dwarf templates.
2. We compare the near-infrared spectra and W1, W2, [3.6], and [4.5] broadband photometry of COCONUTS-2b with 16 state-of-the-art atmospheric model grids of T/Y dwarfs to investigate what model assumptions can better approximate the particular atmosphere of COCONUTS-2b. The most preferred model grids are PH₃-free ATMO2020++, ATMO2020++, and Exo-REM, suggesting the presence of disequilibrium chemistry, along with a diabatic thermal structure and/or clouds, in the atmosphere of COCONUTS-2b.
3. Offsets between data and fitted models are discussed. We find that the predicted Y-band fluxes by all these models are much fainter than the observations, highlighting the uncertainties in the alkali chemistry models and opacities. In addition, all the atmospheric model grids, except for Exo-REM, predict fainter fluxes than the observations

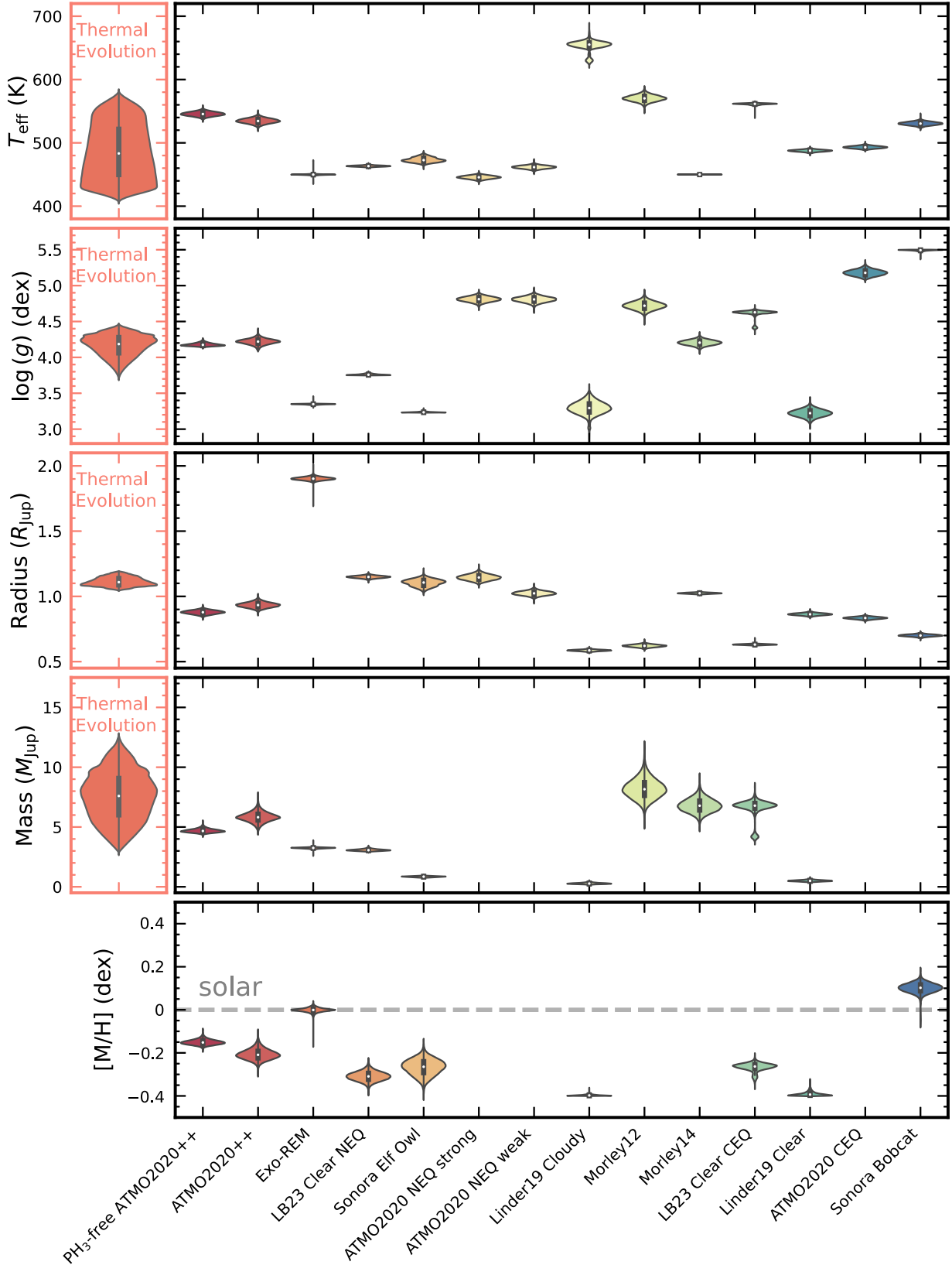


Figure 11. Violin plot for the physical properties of COCONUTS-2b determined from thermal evolution models (the left-hand column; Section 5.4.2) and various atmospheric models using the Gemini/F2 spectrum and $W1/W2[3.6]/[4.5]$ photometry (the right-hand column; Section 4). The evolution-based parameter posteriors are obtained by concatenating the results from several hot-star and cold-start evolution models (Table 4). The plotted atmospheric models are ordered by their corresponding BIC values (low to high from left to right). The spectroscopically inferred masses of the following atmospheric models are between 20 and $70 M_{\text{Jup}}$, and thus outside the y-axis range: ATMO2020 NEQ strong, ATMO2020 NEQ weak, ATMO2020 CEQ, and Sonora Bobcat.

near $3.6\ \mu\text{m}$; the upper-atmospheric heating and/or clouds may play important roles in resolving these offsets. Additionally, we find that (1) the models with chemical equilibrium and no clouds underpredict COCONUTS-2b's fluxes in the H band, (2) the models with chemical equilibrium and clouds yield a broad and faint J -band spectral shape, and (3) the models with disequilibrium chemistry and no clouds underpredict the observed fluxes in the K band. These offsets justify the need for disequilibrium chemistry, modifications to the atmospheric adiabatic index, and clouds in the model assumptions.

4. The forward-modeling analysis is repeated with the Y band excluded or with the $W3$ photometry included. These variations of the input spectrophotometry can lead to changes in the inferred parameters but do not alter our discussions and conclusions.
5. The bolometric luminosity of COCONUTS-2b is computed using spectroscopically inferred T_{eff} and R , with the residuals between observations and fitted models propagated. This leads to $\log(L_{\text{bol}}/L_{\odot}) = -6.18$ dex, with a 0.5 dex wide range of $[-6.43, -5.93]$ dex. This range accounts for the scatter of predicted values across models with different assumptions.
6. Physical properties of COCONUTS-2b are derived based on various thermal evolution models using its bolometric luminosity ($\log(L_{\text{bol}}/L_{\odot}) = [-6.43, -5.93]$ dex) and its parent star's age (150–800 Myr), including $T_{\text{eff}} = 483^{+44}_{-53}\ \text{K}$, $\log(g) = 4.19^{+0.18}_{-0.13}$ dex, $R = 1.11^{+0.03}_{-0.04}\ R_{\text{Jup}}$, $M = 8 \pm 2\ M_{\text{Jup}}$, and a companion-to-host mass ratio of 0.021 ± 0.005 .
7. The spectroscopically inferred physical parameters from several model grids differ from those derived by thermal evolution models. For instance, Exo-REM predicts a 6.5σ lower $\log(g)$ and a 25σ higher radius than the evolution-based estimates. Such discrepancies between atmospheric and evolution models have been reported for other gas-giant exoplanets and brown dwarfs, likely arising from the systematics of model assumptions.
8. Multiple atmospheric model grids consistently suggest that COCONUTS-2b's atmosphere has subsolar or near-solar [M/H] and C/O ratio. These properties provide insights into its formation and potential outward migration; they also suggest that COCONUTS-2b was likely not influenced by core erosion or planetesimal accretion. Furthermore, according to our most preferred model grid, PH₃-free ATMO2020++, the metallicity of COCONUTS-2b ($[\text{M}/\text{H}] = -0.152^{+0.012}_{-0.010}$ dex) is 2σ lower than that of its parent star ($[\text{M}/\text{H}] = 0.00 \pm 0.08$ dex), reducing the likelihood of an in situ, binary-like formation for this planetary-mass companion. However, our third-preferred model grid, Exo-REM, suggests that COCONUTS-2b and 2A have consistent atmospheric metallicities, supporting a binary-like formation pathway.

Looking forward, upcoming JWST observations of COCONUTS-2b (GO programs 2124, 3514, and 6463) will provide higher precision constraints on its atmospheric properties, offering new insights into its disequilibrium chemistry, thermal structure, cloud properties, and atmospheric compositions, further illuminating the formation history of COCONUTS-2b.

Acknowledgments

Z.Z. thanks Benjamin Charnay, Gaël Chauvin, Jackie Faherty, Brianna Lacy, and Eliot Vrijmoet for the helpful discussions. Figure 1 is inspired by Gaël Chauvin's presentation during the conference "Open Problems in the Astrophysics of Gas Giants" in Chile in 2023 December. Z.Z. acknowledges support from the NASA Hubble Fellowship grant HST-HF2-51522.001-A. T.J.D. acknowledges support from UKRI STFC AGP grant ST/W001209/1. We acknowledge the use of the lux supercomputer at UC Santa Cruz, funded by NSF MRI grant AST 1828315. For open access, the author has applied a Creative Commons Attribution (CC BY) license to any Author Accepted Manuscript version arising from this submission. This work is based on observations obtained at the international Gemini Observatory, a program of NSF NOIRLab, which is managed by the Association of Universities for Research in Astronomy (AURA) under a cooperative agreement with the U.S. National Science Foundation on behalf of the Gemini Observatory partnership: the U.S. National Science Foundation (United States), National Research Council (Canada), Agencia Nacional de Investigación y Desarrollo (Chile), Ministerio de Ciencia, Tecnología e Innovación (Argentina), Ministério da Ciência, Tecnologia, Inovações e Comunicações (Brazil), and Korea Astronomy and Space Science Institute (Republic of Korea). This work has benefitted from The UltracoolSheet,²⁶ maintained by Will Best, Trent Dupuy, Michael Liu, Aniket Sanghi, Rob Siverd, and Zhoujian Zhang, and developed from compilations by T. J. Dupuy & M. C. Liu (2012); T. J. Dupuy & A. L. Kraus (2013); M. C. Liu et al. (2016); W. M. J. Best et al. (2018, 2021); A. Sanghi et al. (2023), and A. C. Schneider et al. (2023). This research has benefited from the SpeX Prism Library and the SpeX Prism Library Analysis Toolkit, maintained by Adam Burgasser.²⁷ This research has made use of the NASA Exoplanet Archive, which is operated by the California Institute of Technology, under contract with the National Aeronautics and Space Administration under the Exoplanet Exploration Program. This work used IRAF, as distributed by the National Optical Astronomy Observatory, which is operated by the Association of Universities for Research in Astronomy (AURA) under a cooperative agreement with the National Science Foundation.

Facility: Gemini: South (FLAMINGOS-2).

Software: PyMultiNest (J. Buchner et al. 2014), MultiNest (F. Feroz & M. P. Hobson 2008; F. Feroz et al. 2009, 2019), corner.py (D. Foreman-Mackey 2016), astropy (Astropy Collaboration et al. 2013, 2018, 2022), ipython (F. Pérez & B. E. Granger 2007), numpy (C. R. Harris et al. 2020), scipy (P. Virtanen et al. 2020), matplotlib (J. D. Hunter 2007).

Appendix A Comparison of the Gemini/F2 Spectroscopy and an Archival Spectrum

We compare our Gemini/F2 spectrum with an archival near-infrared spectrum obtained by J. D. Kirkpatrick et al. (2011) on 2010 April 3 UT, before Z. Zhang et al. (2021a) discovered that this previously thought free-floating brown dwarf is instead a planetary-mass companion of the young star COCONUTS-2A. The archival spectrum ($R \sim 300$) was collected using the

²⁶ <http://bit.ly/UltracoolSheet>

²⁷ <https://splat.physics.ucsd.edu/splat/>

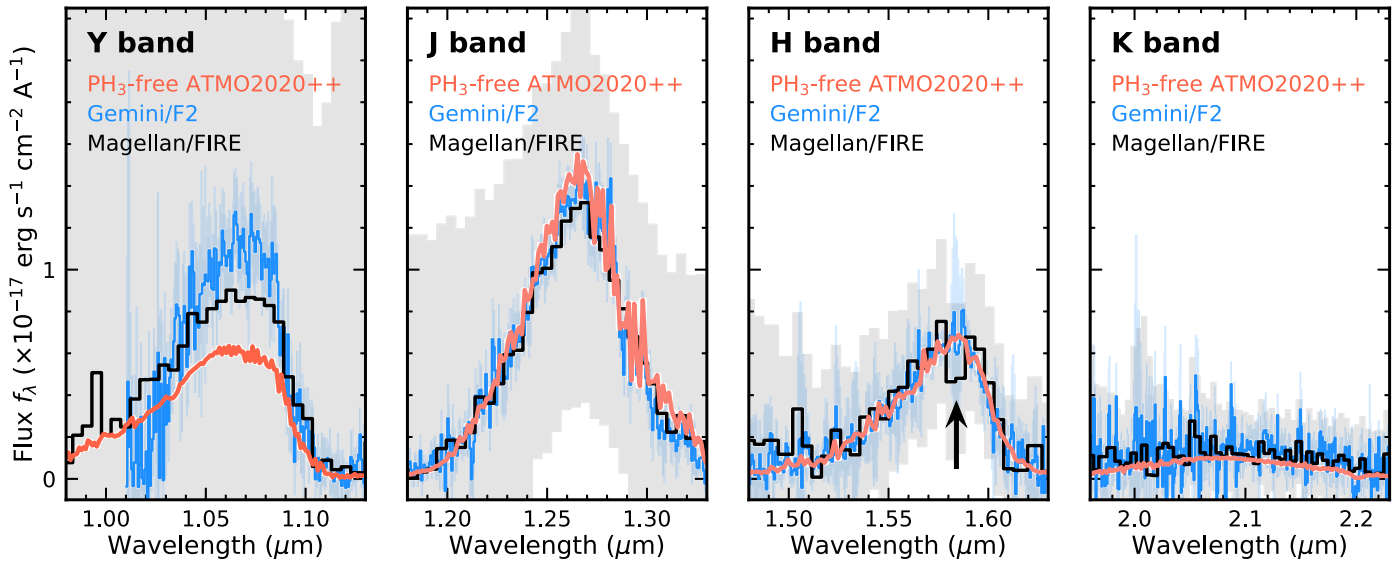


Figure 12. Comparison of the Gemini/F2 spectrum of COCONUTS-2b (blue) with the archival Magellan/FIRE spectrum (black) across the Y , J , H , and K bands, with 1σ flux uncertainties highlighted by colored shades. Both spectra are flux-calibrated using the same J -band magnitude (see Section 2). The maximum-likelihood PH_3 -free ATMO2020++ model spectrum (orange), as shown in Figure 4, is overlaid for comparison. The Magellan/FIRE spectrum exhibits an absorption feature in the H band (marked by an arrow symbol), which is absent in the Gemini/F2 spectrum with a higher S/N and spectral resolution.

Folded-port Infrared Echellette (FIRE; R. A. Simcoe et al. 2008) mounted on the 6.5 m Magellan Baade Telescope. The Magellan/FIRE spectrum has a signal-to-noise ratio (S/N) of ≈ 0.5 , ≈ 1.4 , ≈ 2.0 , and ≈ 1.0 per pixel near the peak of the Y , J , H , and K band, respectively; these values are greatly lower than the quality of our Gemini/F2 spectrum, which has an S/N of ≈ 6 in Y band, ≈ 10 in J band, ≈ 8 in H band, and ≈ 2 in K band. As shown in Figure 12, the Gemini/F2 and Magellan/FIRE spectra of COCONUTS-2b are generally consistent.

When comparing our Gemini/F2 spectrum with the median spectral fluxes of Magellan/FIRE, we find that the latter spectrum shows slightly fainter fluxes near the peak of the Y band (1.05 – 1.09 μm); this difference is not significant given the flux uncertainties of the Magellan/FIRE spectrum. We also note that the Y -band fluxes of the Gemini/F2 spectrum over the wavelength range of 1.05 – 1.09 μm remain stable, despite variations in data reduction setups. Extracting COCONUTS-2b’s Gemini/F2 spectra using the object’s own spectral trace (which is not recommended for our target; see Section 2 and S. K. Leggett et al. 2016a) instead of using the standard star as a reference (as done in Section 2) results in fainter Y -band fluxes by only $\sim 0.5\sigma$ over a narrow wavelength range of 1.07 – 1.09 μm . However, at wavelengths below ≈ 1.03 μm , the Gemini/F2 spectral fluxes are likely affected by the comprised accuracy of the sensitivity function near the detector edge. Additionally, in the H band, the archival spectrum exhibits an absorption feature near 1.58 μm that is absent in the Gemini/F2 spectrum, which has a higher S/N and spectral resolution. In

summary, our Gemini/F2 spectrum provides a higher-quality set of near-infrared spectroscopy for COCONUTS-2b compared to the archival data.

Appendix B χ^2 -based Spectral Fits with the LB23 Cloudy Models

We compare the Gemini/F2 spectrum of COCONUTS-2b with all the LB23 Cloudy CEQ and NEQ models over the wavelengths of 1.05 – 1.12 μm , 1.18 – 1.35 μm , 1.45 – 1.66 μm , and 1.95 – 2.30 μm (Section 4.2). A χ^2 value of each model is computed by comparing the observed fluxes with the model spectrum scaled by a factor of α , as defined in Equation (2) of M. W. Phillips et al. (2024). The scaling factor corresponding to the best-fit model is then used to derive the planet’s radius as $R = d\sqrt{\alpha}$, with $d = 10.888$ pc.

Figure 13 presents our results, including the best-fitted model spectra, data-model residuals, and the χ^2 over the parameter space of each model grid. The χ^2 values of these models decrease toward hotter effective temperatures, suggesting that COCONUTS-2b’s T_{eff} is beyond the parameter space of these models. Additionally, the publicly available LB23 Cloudy models include two versions of clouds: “AEE10” and “E10.” Both models assume a cloud particle size of 10 μm , but the former version assumes a more vertically extended cloud layer (see Section 2.3 of B. Lacy & A. Burrows 2023a), which we find can better match the spectroscopy of COCONUTS-2b.

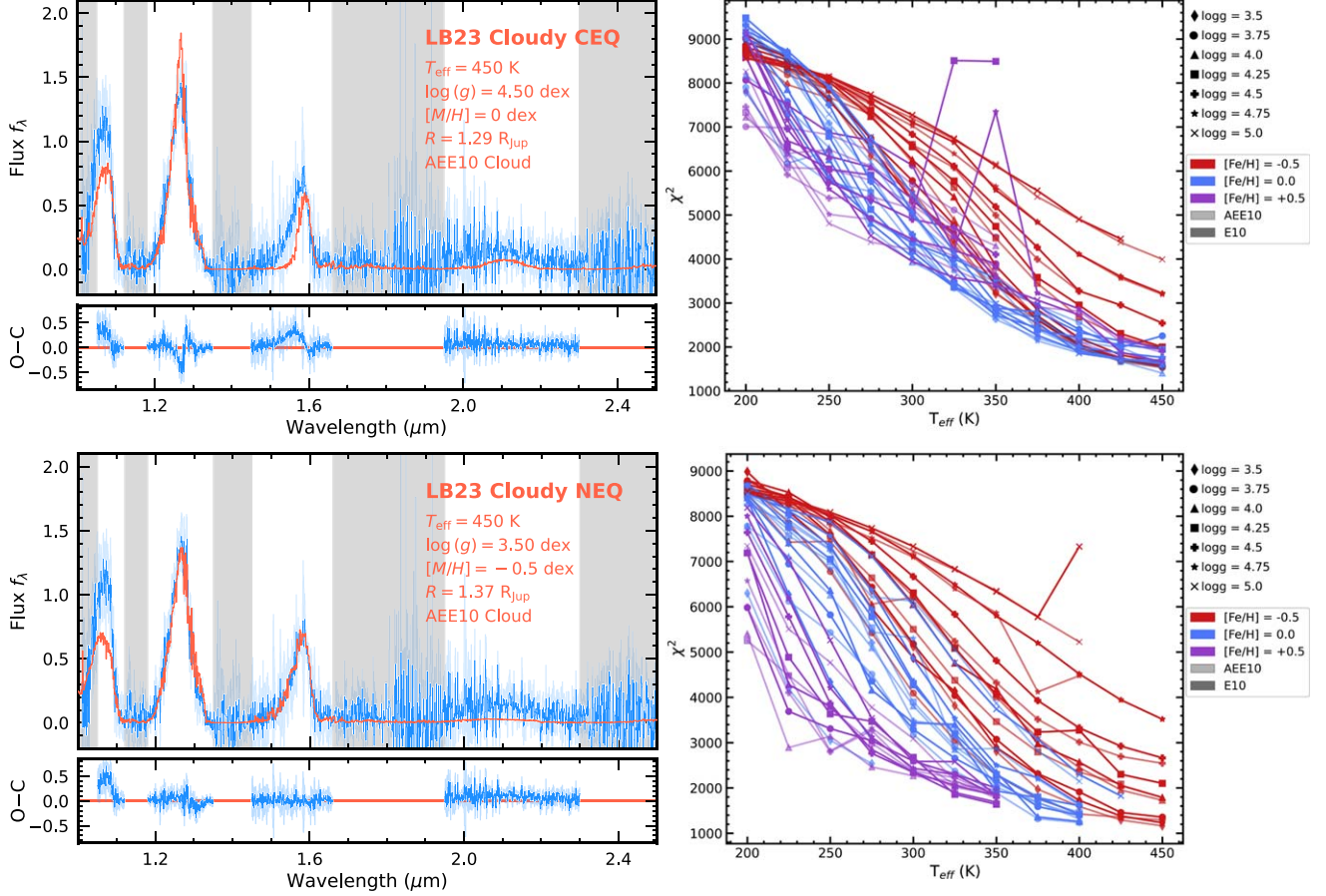


Figure 13. Top panels: χ^2 -based spectral fitting results using the LB23 Cloudy CEQ grid. The top left-hand panel presents the observed Gemini/F2 spectrum of COCONUTS-2b (blue) overlaid with the best-fit model spectrum (orange). The best-fitted physical parameters are labeled. The gray-shaded regions indicate the masked wavelength regions. The bottom left-hand panel presents the data-model residuals. The right-hand panel presents our computed χ^2 for a given set of grid parameters, including T_{eff} , $\log(g)$, $[M/H]$, and cloud properties (AEE10 or E10). Bottom panels: Spectral fits with the LB23 Cloudy NEQ grid, with the same format as the top row.

Appendix C Forward-modeling Analyses with Different Portions of the Spectrophotometry

Figure 14 presents the results of our forward-modeling analysis with the Y -band Gemini/F2 spectrum fully masked.

Figure 15 presents the results with the $W3$ photometry included. The confidence intervals of inferred parameters are summarized in Tables 2 and 3.

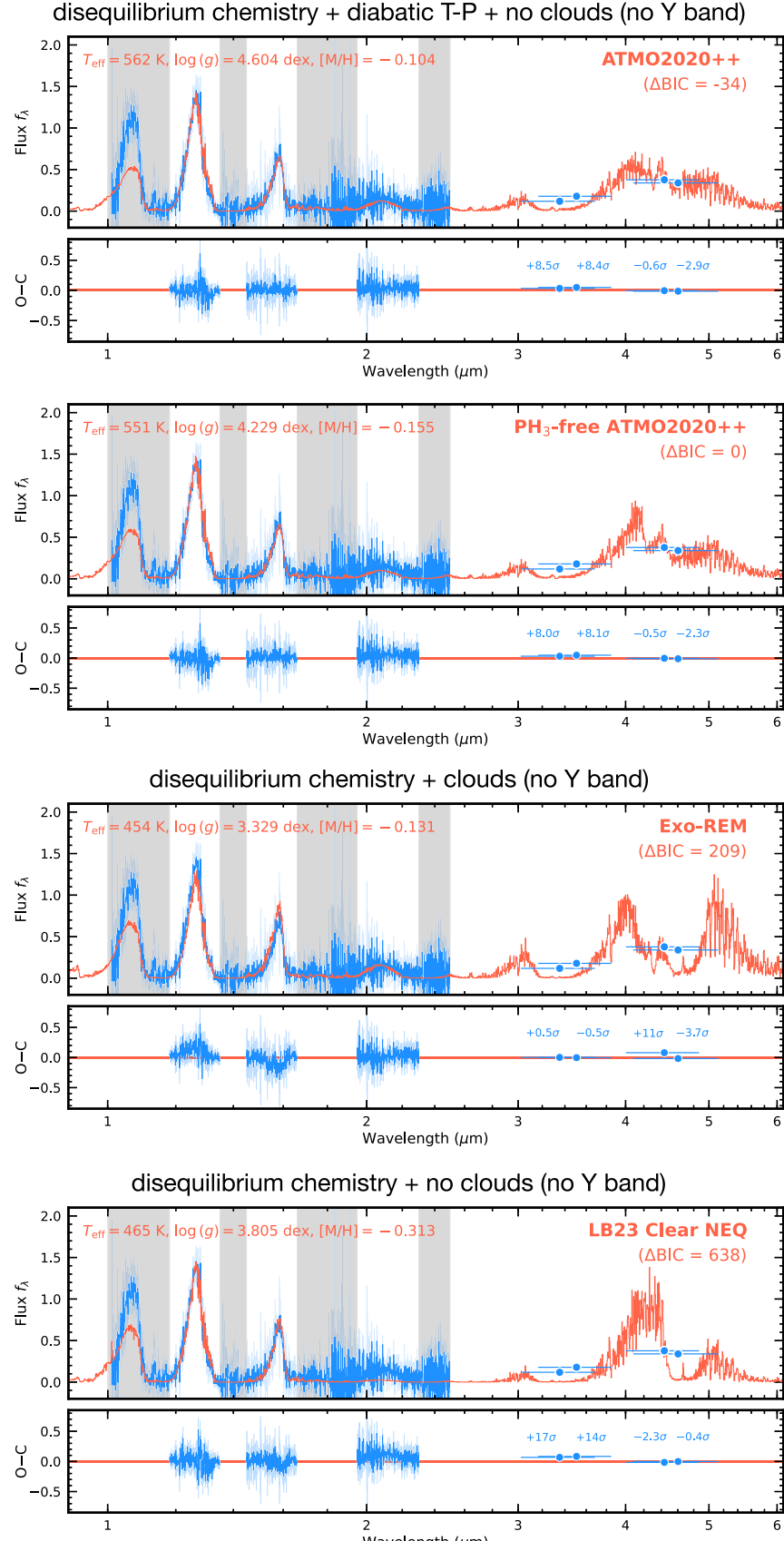


Figure 14. Forward-modeling analysis results with the Y -band Gemini/F2 spectrum fully masked. The format is the same as Figure 4.

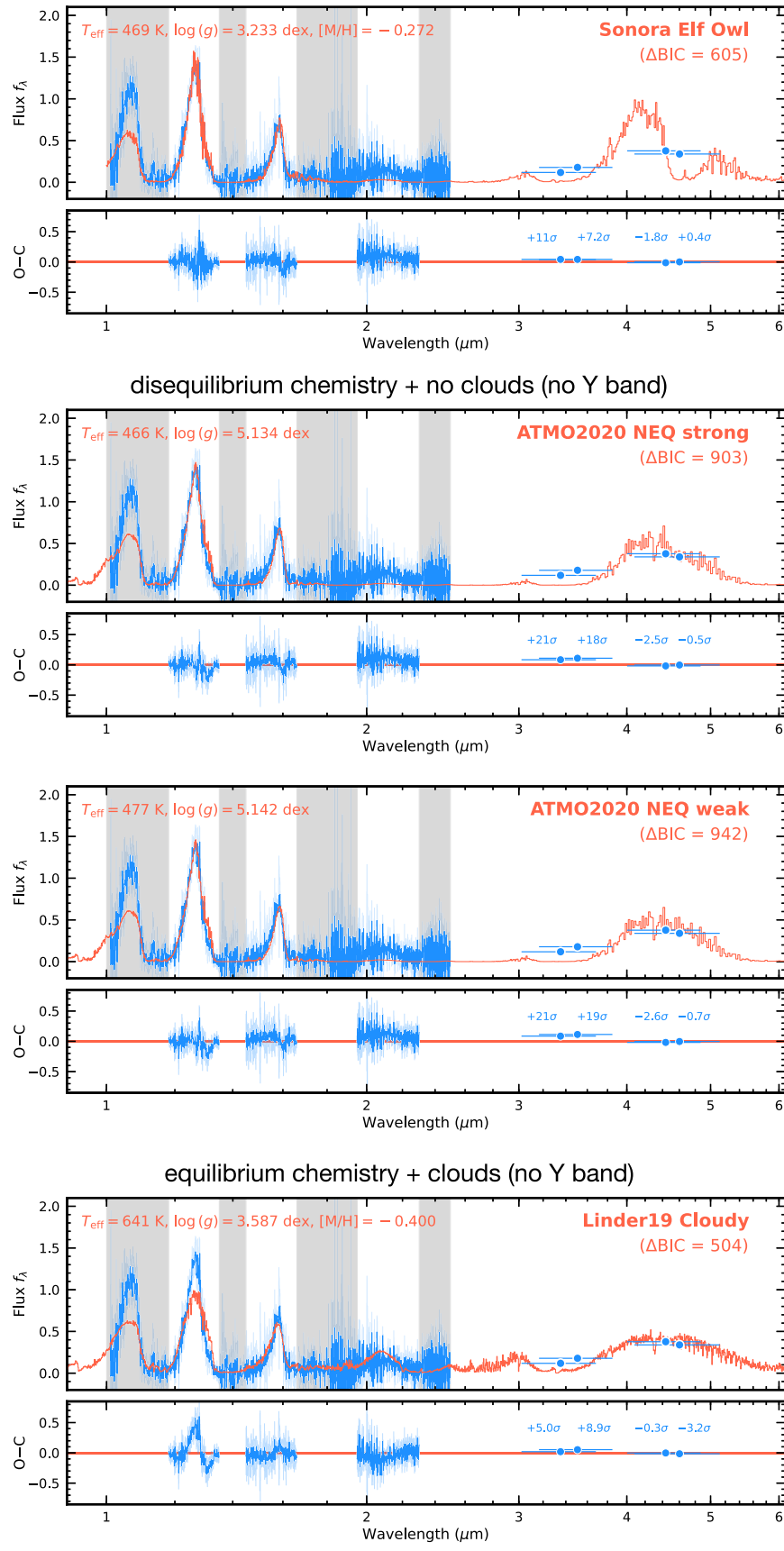
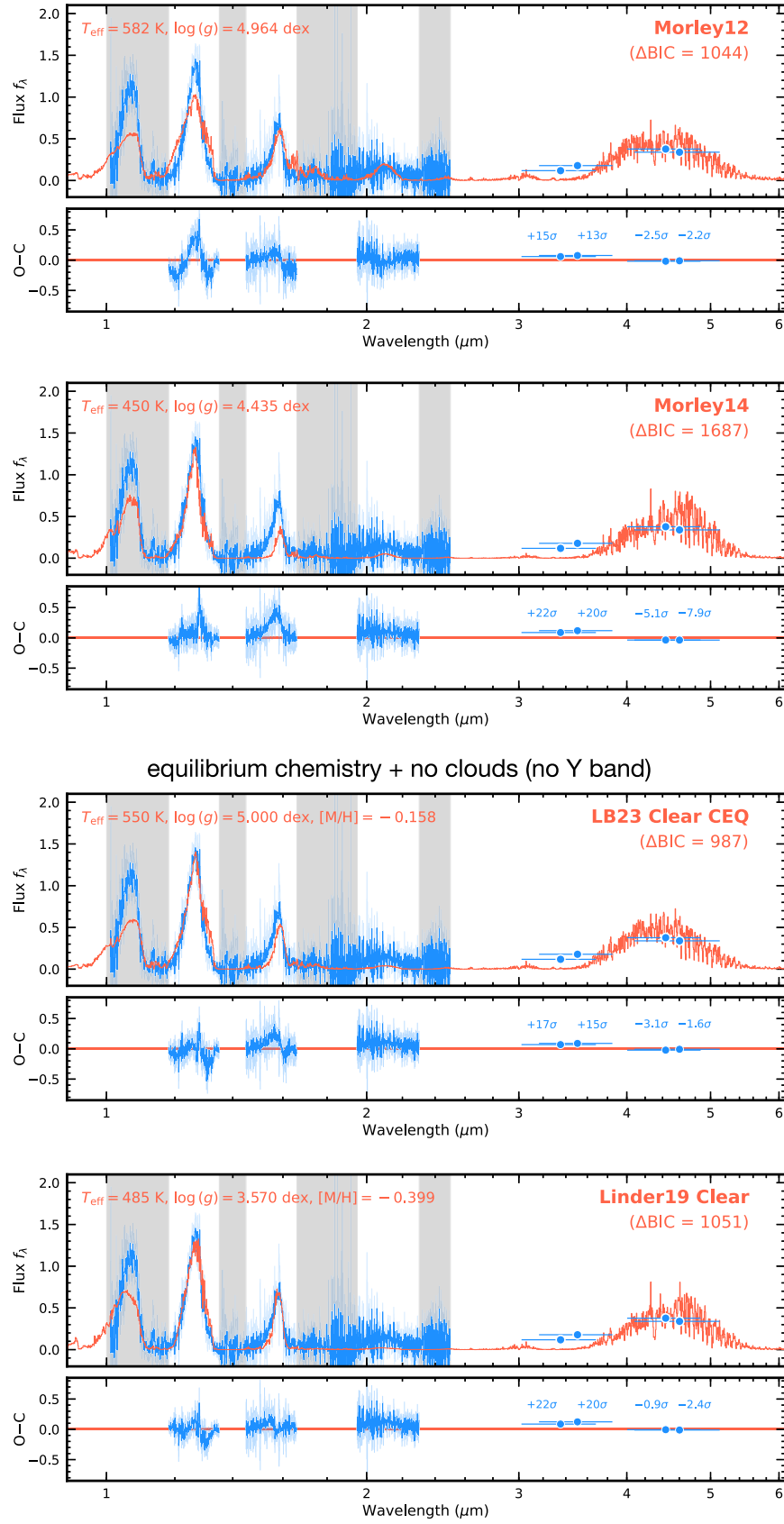
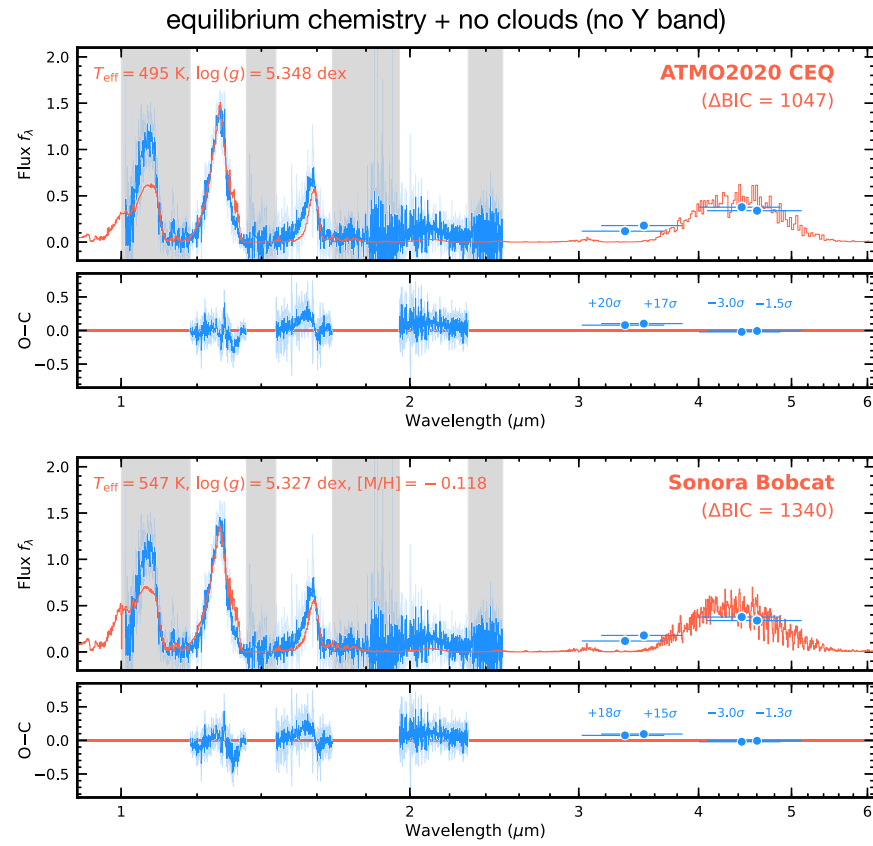
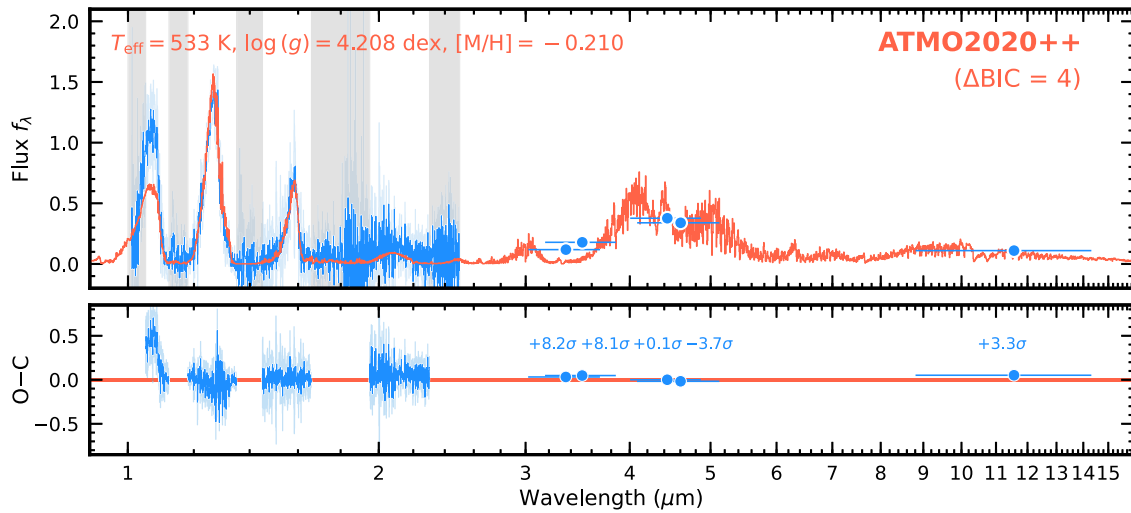
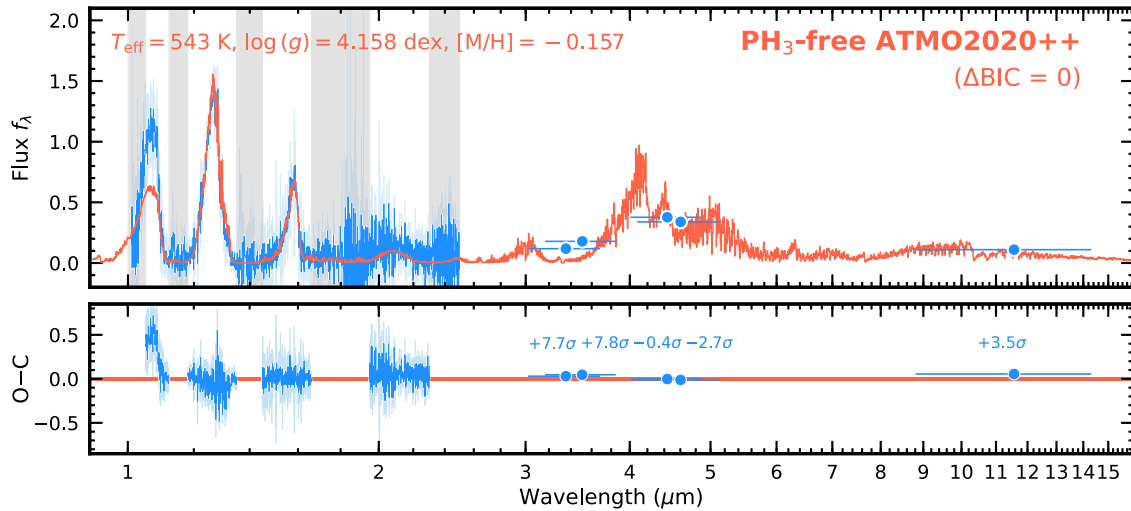


Figure 14. (Continued.)

**Figure 14.** (Continued.)

**Figure 14.** (Continued.)

disequilibrium chemistry + diabatic T-P + no clouds (W3 included)



disequilibrium chemistry + clouds (W3 included)

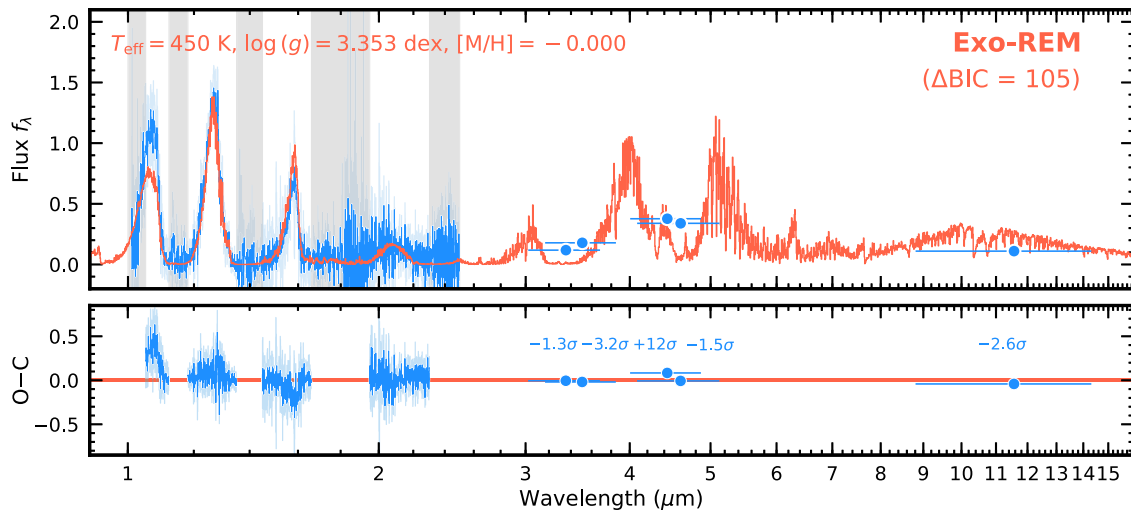
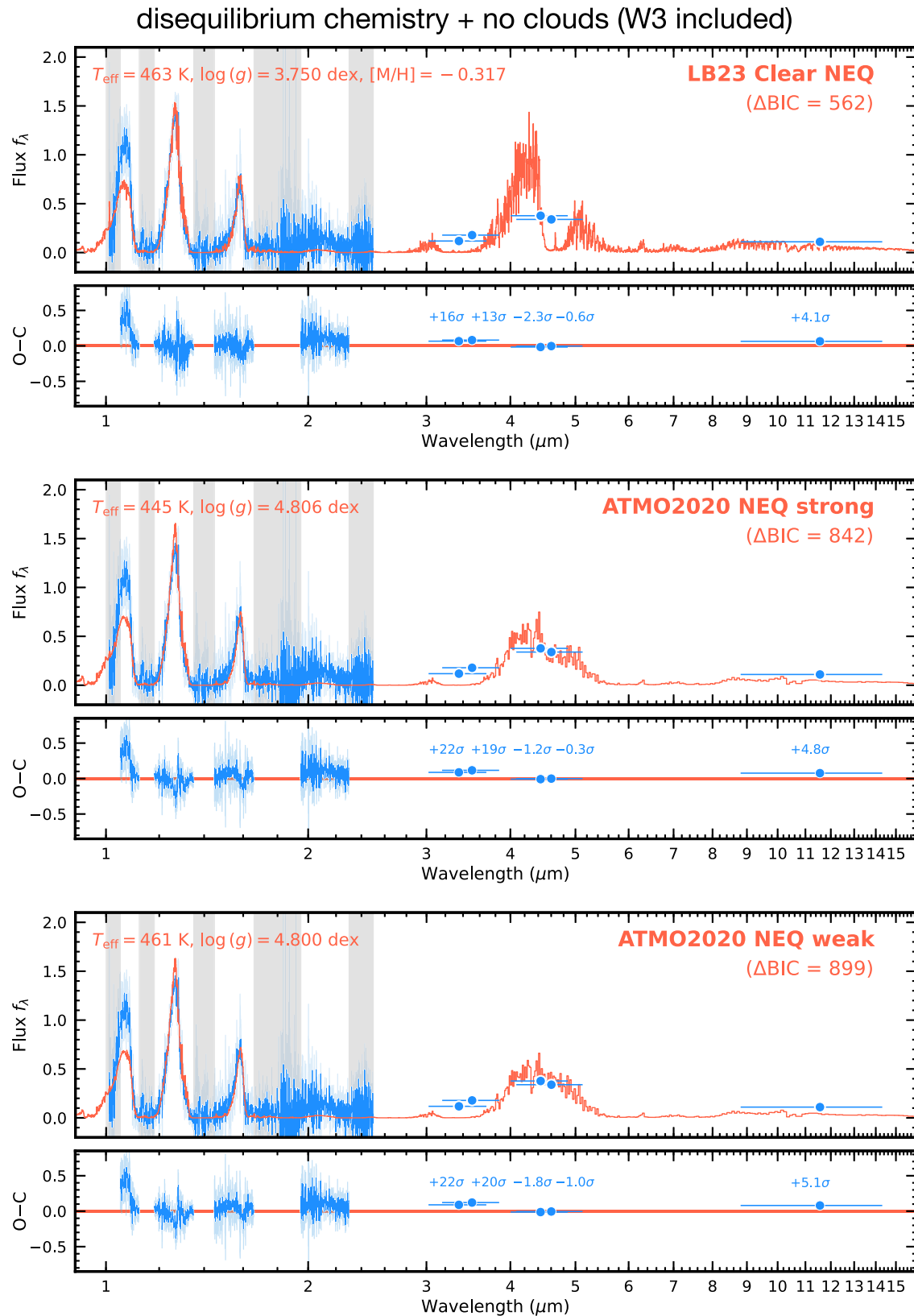


Figure 15. Forward-modeling analysis results with the W3 photometry included. The format is the same as Figure 4.

**Figure 15.** (Continued.)

equilibrium chemistry + clouds (W3 included)

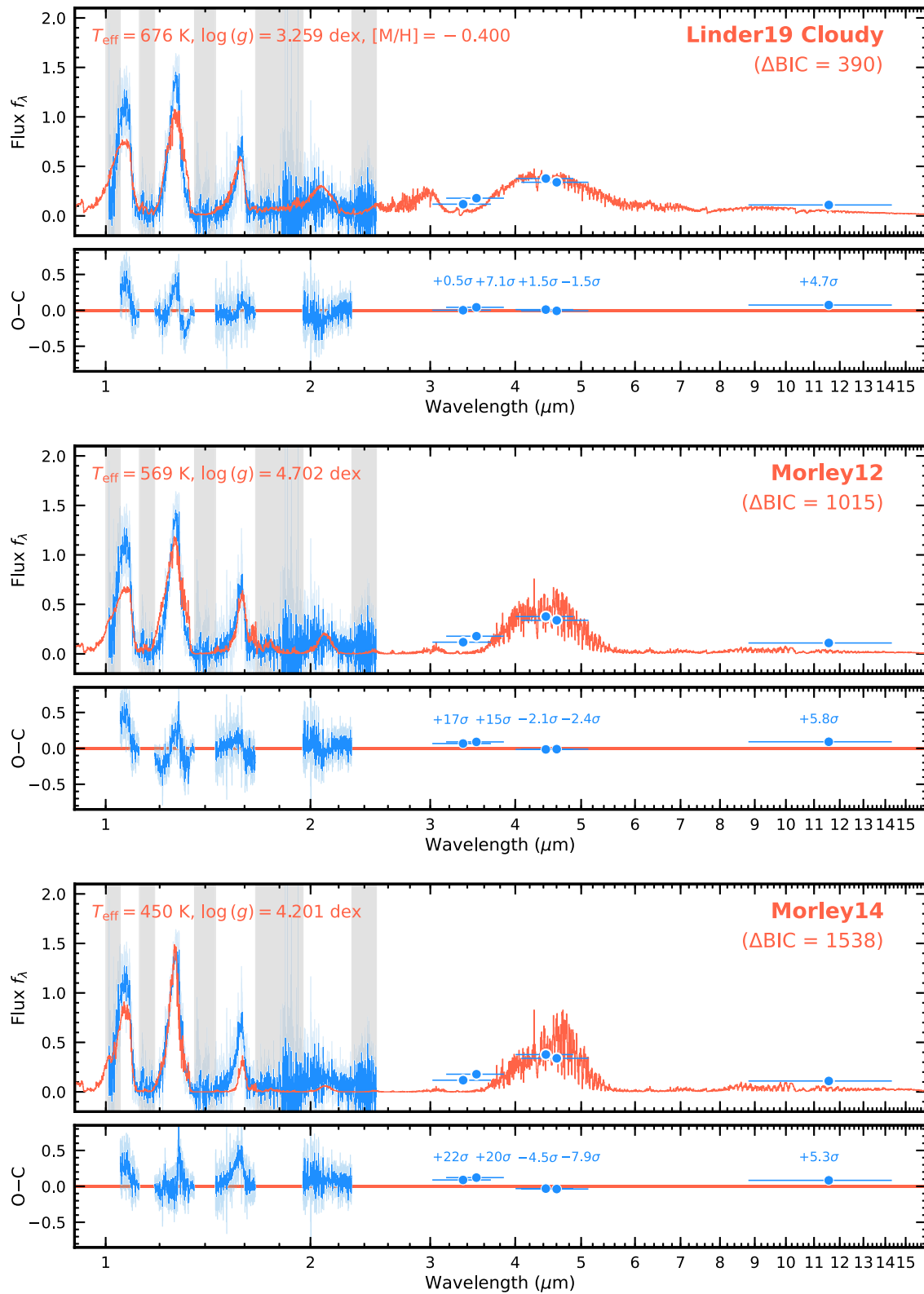


Figure 15. (Continued.)

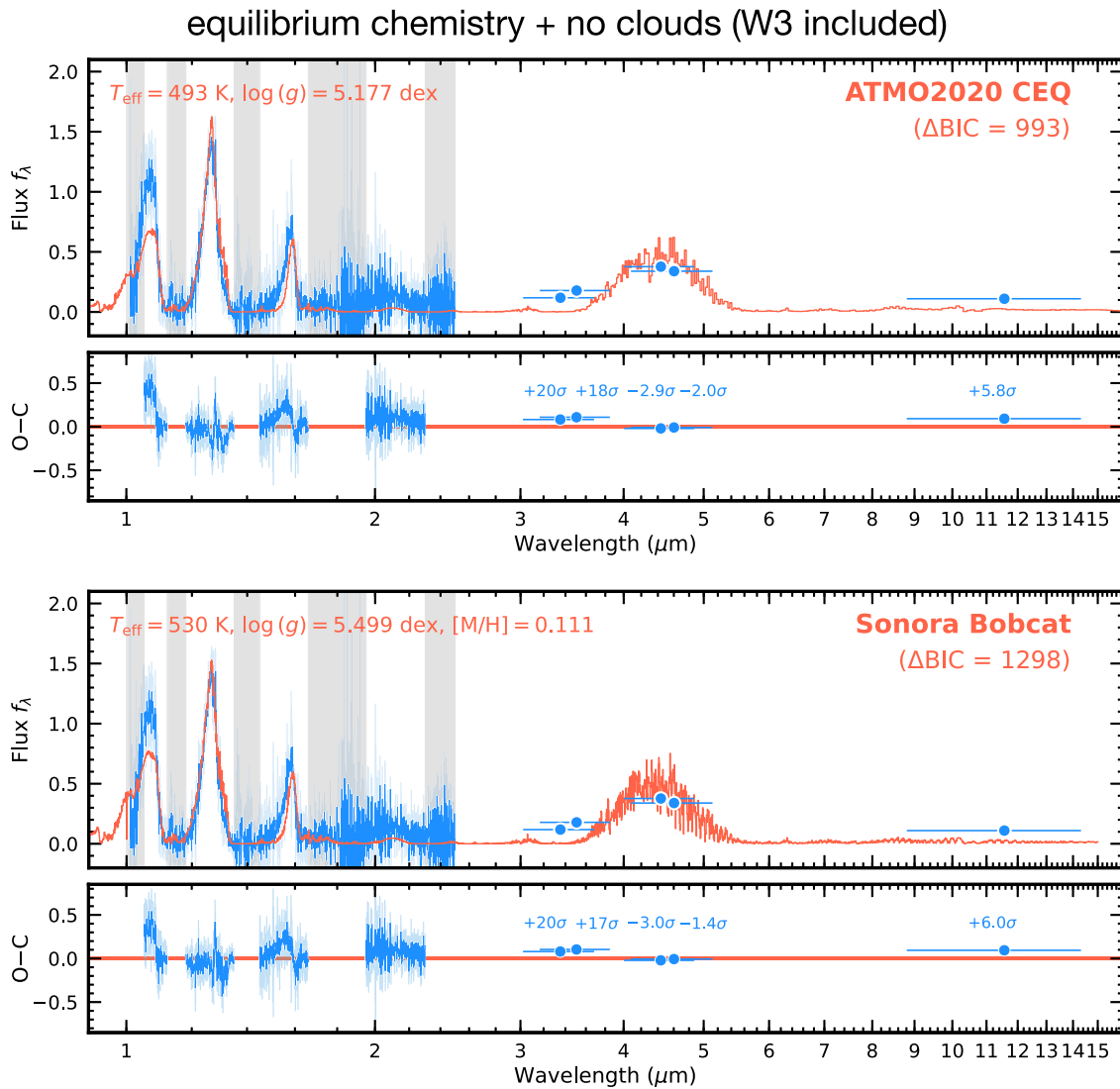


Figure 15. (Continued.)

ORCID iDs

- Zhoujian Zhang (张周健) <https://orcid.org/0000-0002-3726-4881>
- Sagnick Mukherjee <https://orcid.org/0000-0003-1622-1302>
- Michael C. Liu <https://orcid.org/0000-0003-2232-7664>
- Jonathan J. Fortney <https://orcid.org/0000-0002-9843-4354>
- Emily Mader <https://orcid.org/0009-0002-9013-8005>
- William M. J. Best <https://orcid.org/0000-0003-0562-1511>
- Trent J. Dupuy <https://orcid.org/0000-0001-9823-1445>
- Sandy K. Leggett <https://orcid.org/0000-0002-3681-2989>
- Theodora Karalidi <https://orcid.org/0000-0001-7356-6652>
- Michael R. Line <https://orcid.org/0000-0002-2338-476X>
- Mark S. Marley <https://orcid.org/0000-0002-5251-2943>
- Caroline V. Morley <https://orcid.org/0000-0002-4404-0456>
- Mark W. Phillips <https://orcid.org/0000-0001-6041-7092>
- Robert J. Siverd <https://orcid.org/0000-0001-5016-3359>
- Joseph A. Zalesky <https://orcid.org/0000-0001-9828-1848>

References

- Ackerman, A. S., & Marley, M. S. 2001, *ApJ*, 556, 872
- Alderson, L., Wakeford, H. R., Alam, M. K., et al. 2023, *Natur*, 614, 664
- Alibert, Y., Mousis, O., & Benz, W. 2005, *ApJL*, 622, L145
- Allard, N. F., Allard, F., Hauschildt, P. H., Kielkopf, J. F., & Machin, L. 2003, *A&A*, 411, L473
- Allard, N. F., Spiegelman, F., & Kielkopf, J. F. 2016, *A&A*, 589, A21
- Allard, N. F., Spiegelman, F., Leininger, T., & Molliere, P. 2019, *A&A*, 628, A120
- Apai, D., Karalidi, T., Marley, M. S., et al. 2017, *Sci*, 357, 683
- Artigau, É., Bouchard, S., Doyon, R., & Lafrenière, D. 2009, *ApJ*, 701, 1534
- Asplund, M., Grevesse, N., & Sauval, A. J. 2006, *CoAst*, 147, 76
- Asplund, M., Grevesse, N., Sauval, A. J., & Scott, P. 2009, *ARA&A*, 47, 481
- Astropy Collaboration, Robitaille, T. P., Tollerud, E. J., et al. 2013, *A&A*, 558, A33
- Astropy Collaboration, Price-Whelan, A. M., Sipőcz, B. M., et al. 2018, *AJ*, 156, 123
- Astropy Collaboration, Price-Whelan, A. M., Lim, P. L., et al. 2022, *ApJ*, 935, 167
- August, P. C., Bean, J. L., Zhang, M., et al. 2023, *ApJL*, 953, L24
- Bailer-Jones, C. A. L., Rybizki, J., Fouesneau, M., Demleitner, M., & Andrae, R. 2021, *AJ*, 161, 147
- Barrado, D., Mollière, P., Patapis, P., et al. 2023, *Natur*, 624, 263
- Baudino, J. L., Bézard, B., Boccaletti, A., et al. 2015, *A&A*, 582, A83
- Bean, J. L., Xue, Q., August, P. C., et al. 2023, *Natur*, 618, 43
- Beiler, S. A., Cushing, M. C., Kirkpatrick, J. D., et al. 2023, *ApJL*, 951, L48
- Beiler, S. A., Cushing, M. C., Kirkpatrick, J. D., et al. 2024, *ApJ*, 973, 107
- Best, W. M. J., Dupuy, T. J., Liu, M. C., et al. 2024a, *The UltracoolSheet: Photometry, Astrometry, Spectroscopy, and Multiplicity for 4000+*

- Ultracool Dwarfs and Imaged Exoplanets, v2.0.0, Zenodo, doi:10.5281/zenodo.1057324
- Best, W. M. J., Liu, M. C., Magnier, E. A., & Dupuy, T. J. 2020, *AJ*, 159, 257
- Best, W. M. J., Liu, M. C., Magnier, E. A., & Dupuy, T. J. 2021, *AJ*, 161, 42
- Best, W. M. J., Sanghi, A., Liu, M. C., Magnier, E. A., & Dupuy, T. J. 2024b, *ApJ*, 967, 115
- Best, W. M. J., Liu, M. C., Magnier, E. A., et al. 2015, *ApJ*, 814, 118
- Best, W. M. J., Magnier, E. A., Liu, M. C., et al. 2018, *ApJS*, 234, 1
- Blain, D., Charnay, B., & Bézard, B. 2021, *A&A*, 646, A15
- Bochanski, J. J., Burgasser, A. J., Simcoe, R. A., & West, A. A. 2011, *AJ*, 142, 169
- Bowler, B. P. 2016, *PASP*, 128, 102001
- Bowler, B. P., Zhou, Y., Morley, C. V., et al. 2020, *ApJL*, 893, L30
- Bowler, B. P., Tran, Q. H., Zhang, Z., et al. 2023, *AJ*, 165, 164
- Buchner, J., Georgakakis, A., Nandra, K., et al. 2014, *A&A*, 564, A125
- Burgasser, A. J. 2014, in *ASI Conf. Ser.* 11, *Int. Workshop on Stellar Spectral Libraries*, ed. H. P. Singh et al. (Hyderabad: ASI), 7
- Burningham, B., Marley, M. S., Line, M. R., et al. 2017, *MNRAS*, 470, 1177
- Burrows, A., Hubbard, W. B., & Lunine, J. I. 1989, *ApJ*, 345, 939
- Burrows, A., Hubbard, W. B., Lunine, J. I., & Liebert, J. 2001, *RvMP*, 73, 719
- Burrows, A., & Volobuyev, M. 2003, *ApJ*, 583, 985
- Caffau, E., Ludwig, H. G., Steffen, M., Freytag, B., & Bonifacio, P. 2011, *SofPh*, 268, 255
- Chabrier, G., Baraffe, I., Phillips, M., & Debras, F. 2023, *A&A*, 671, A119
- Charnay, B., Bézard, B., Baudino, J. L., et al. 2018, *ApJ*, 854, 172
- Coulombe, L.-P., Benneke, B., Challener, R., et al. 2023, *Natur*, 620, 292
- Currie, T., Biller, B., Lagrange, A., et al. 2023, in *ASP Conf. Ser.* 534, *Protostars and Planets VII*, ed. S. Inutsuka et al. (San Francisco, CA: ASP), 799
- Cushing, M. C., Marley, M. S., Saumon, D., et al. 2008, *ApJ*, 678, 1372
- Cushing, M. C., Kirkpatrick, J. D., Gelino, C. R., et al. 2011, *ApJ*, 743, 50
- Cushing, M. C., Hardegree-Ullman, K. K., Trucks, J. L., et al. 2016, *ApJ*, 823, 152
- Cutri, R. M., Wright, E. L., Conrow, T., et al. 2021, *yCat*, II/328
- Czekala, I., Andrews, S. M., Mandel, K. S., Hogg, D. W., & Green, G. M. 2015, *ApJ*, 812, 128
- De Rosa, R. J., Nielsen, E. L., Wahhaj, Z., et al. 2023, *A&A*, 672, A94
- Deacon, N. R., Schlieder, J. E., & Murphy, S. J. 2016, *MNRAS*, 457, 3191
- Dupuy, T. J., Brandt, G. M., & Brandt, T. D. 2022, *MNRAS*, 509, 4411
- Dupuy, T. J., Forbrich, J., Rizzato, A., et al. 2016, *ApJ*, 827, 23
- Dupuy, T. J., & Kraus, A. L. 2013, *Sci*, 341, 1492
- Dupuy, T. J., & Liu, M. C. 2012, *ApJS*, 201, 19
- Dupuy, T. J., & Liu, M. C. 2017, *ApJS*, 231, 15
- Dupuy, T. J., Liu, M. C., Evans, E. L., et al. 2023, *MNRAS*, 519, 1688
- Dupuy, T. J., Liu, M. C., Best, W. M. J., et al. 2019, *AJ*, 158, 174
- Eikenberry, S., Elston, R., Raines, S. N., et al. 2008, *Proc. SPIE*, 7014, 70140V
- Eikenberry, S. S., Elston, R., Raines, S. N., et al. 2004, *Proc. SPIE*, 5492, 1196
- Eisenhardt, P. R. M., Marocco, F., Fowler, J. W., et al. 2020, *ApJS*, 247, 69
- Esplin, T. L., Luhman, K. L., Cushing, M. C., et al. 2016, *ApJ*, 832, 58
- Faherty, J. K., Burningham, B., Gagné, J., et al. 2024, *Natur*, 628, 511
- Fegley, B. J., & Lodders, K. 1996, *ApJL*, 472, L37
- Feinstein, A. D., Radica, M., Welbanks, L., et al. 2023, *Natur*, 614, 670
- Feroz, F., & Hobson, M. P. 2008, *MNRAS*, 384, 449
- Feroz, F., Hobson, M. P., & Bridges, M. 2009, *MNRAS*, 398, 1601
- Feroz, F., Hobson, M. P., Cameron, E., & Pettitt, A. N. 2019, *OJAp*, 2, 10
- Foreman-Mackey, D. 2016, *JOSS*, 1, 24
- Fortney, J. J. 2005, *MNRAS*, 364, 649
- Fortney, J. J. 2018, arXiv:1804.08149
- Franson, K., Bowler, B. P., Zhou, Y., et al. 2023, *ApJL*, 950, L19
- Gagné, J., Faherty, J. K., & Popinchalk, M. 2020, *RNAAS*, 4, 92
- Gagné, J., Mamajek, E. E., Malo, L., et al. 2018, *ApJ*, 856, 23
- Gaia Collaboration, Brown, A. G. A., Vallenari, A., et al. 2016, *A&A*, 595, A2
- Gaia Collaboration, Brown, A. G. A., Vallenari, A., et al. 2021, *A&A*, 649, A1
- Gao, P., Wakeford, H. R., Moran, S. E., & Parmentier, V. 2021, *JGRE*, 126, e06655
- Gonzales, E. C., Burningham, B., Faherty, J. K., et al. 2020, *ApJ*, 905, 46
- GRAVITY Collaboration, Nowak, M., Lacour, S., et al. 2020, *A&A*, 633, A110
- Guillot, T., Chabrier, G., Morel, P., & Gautier, D. 1994, *Icar*, 112, 354
- Gully-Santiago, M., Morley, C. V., Luna, J., et al. 2024, *AJ*, 167, 142
- Hammond, M., Bell, T. J., Challener, R. C., et al. 2024, *AJ*, 168, 4
- Harris, C. R., Millman, K. J., van der Walt, S. J., et al. 2020, *Natur*, 585, 357
- Hoch, K. K. W., Konopacky, Q. M., Theissen, C. A., et al. 2023, *AJ*, 166, 85
- Hojjatpanah, S., Figueira, P., Santos, N. C., et al. 2019, *A&A*, 629, A80
- Hood, C. E., Fortney, J. J., Line, M. R., & Faherty, J. K. 2023, *ApJ*, 953, 170
- Hora, J. L., Carey, S., Surace, J., et al. 2008, *PASP*, 120, 1233
- Hunter, J. D. 2007, *CSE*, 9, 90
- Hurt, S. A., Liu, M. C., Zhang, Z., et al. 2024, *ApJ*, 961, 121
- Inglis, J., Wallack, N. L., Xuan, J. W., et al. 2024, *AJ*, 167, 218
- Jarrett, T. H., Cohen, M., Masci, F., et al. 2011, *ApJ*, 735, 112
- JWST Transiting Exoplanet Community Early Release Science Team, Ahrer, E.-M., Alderson, L., et al. 2023, *Natur*, 614, 649
- Kalalidi, T., Marley, M., Fortney, J. J., et al. 2021, *ApJ*, 923, 269
- Kass, R. E., & Raftery, A. E. 1995, *JASA*, 90, 773
- Kempton, E. M.-R., & Knutson, H. A. 2024, *RvMG*, 90, 411
- Kirkpatrick, J. D., Cushing, M. C., Gelino, C. R., et al. 2011, *ApJS*, 197, 19
- Kirkpatrick, J. D., Gelino, C. R., Cushing, M. C., et al. 2012, *ApJ*, 753, 156
- Kirkpatrick, J. D., Martin, E. C., Smart, R. L., et al. 2019, *ApJS*, 240, 19
- Kirkpatrick, J. D., Gelino, C. R., Faherty, J. K., et al. 2021, *ApJS*, 253, 7
- Kothari, H., Cushing, M. C., Burningham, B., et al. 2024, *ApJ*, 971, 121
- Lacy, B., & Burrows, A. 2023a, *ApJ*, 950, 8
- Lacy, B., & Burrows, A. 2023b, *Self-consistent Models of Y Dwarf Atmospheres with Water Clouds and Disequilibrium Chemistry*, v1.0.0, Zenodo, doi:10.5281/zenodo.7779180
- Lazorenko, P. F., & Sahlmann, J. 2018, *A&A*, 618, A111
- Leggett, S. K., Marley, M. S., Freedman, R., et al. 2007, *ApJ*, 667, 537
- Leggett, S. K., & Tremblin, P. 2023, *ApJ*, 959, 86
- Leggett, S. K., & Tremblin, P. 2024, *RNAAS*, 8, 13
- Leggett, S. K., Tremblin, P., Esplin, T. L., Luhman, K. L., & Morley, C. V. 2017, *ApJ*, 842, 118
- Leggett, S. K., Tremblin, P., Saumon, D., et al. 2016a, *ApJ*, 824, 2
- Leggett, S. K., Cushing, M. C., Hardegree-Ullman, K. K., et al. 2016b, *ApJ*, 830, 141
- Leggett, S. K., Dupuy, T. J., Morley, C. V., et al. 2019, *ApJ*, 882, 117
- Leggett, S. K., Tremblin, P., Phillips, M. W., et al. 2021, *ApJ*, 918, 111
- Lew, B. W. P., Apai, D., Zhou, Y., et al. 2020, *AJ*, 159, 125
- Lew, B. W. P., Roellig, T., Batalha, N. E., et al. 2024, *AJ*, 167, 237
- Liddle, A. R. 2007, *MNRAS*, 377, L74
- Linder, E. F., Mordasini, C., Mollière, P., et al. 2019, *A&A*, 623, A85
- Line, M. R., Marley, M. S., Liu, M. C., et al. 2017, *ApJ*, 848, 83
- Line, M. R., Brogi, M., Bean, J. L., et al. 2021, *Natur*, 598, 580
- Liu, M. C., Dupuy, T. J., & Allers, K. N. 2016, *ApJ*, 833, 96
- Liu, M. C., Delorme, P., Dupuy, T. J., et al. 2011, *ApJ*, 740, 108
- Liu, P., Biller, B. A., Vos, J. M., et al. 2024, *MNRAS*, 527, 6624
- Lodders, K. 1999, *ApJ*, 519, 793
- Lodders, K. 2003, *ApJ*, 591, 1220
- Lodders, K. 2010a, *ASSP*, 16, 379
- Lodders, K. 2010b, *Formation and Evolution of Exoplanets* (New York: Wiley), 157
- Lodders, K., & Fegley, B. J. 2006, in *Astrophysics Update 2*, ed. J. W. Mason (Chichester: Praxis Publishing Ltd), 1
- Lucas, P. W., Tinney, C. G., Burningham, B., et al. 2010, *MNRAS*, 408, L56
- Lueber, A., Kitzmann, D., Bowler, B. P., Burgasser, A. J., & Heng, K. 2022, *ApJ*, 930, 136
- Luhman, K. L., Burgasser, A. J., & Bochanski, J. J. 2011, *ApJL*, 730, L9
- Luhman, K. L., Tremblin, P., Alves de Oliveira, C., et al. 2024, *AJ*, 167, 5
- Lustig-Yaeger, J., Fu, G., May, E. M., et al. 2023, *NatAs*, 7, 1317
- Mace, G. N., Kirkpatrick, J. D., Cushing, M. C., et al. 2013, *ApJS*, 205, 6
- Macintosh, B., Graham, J. R., Barman, T., et al. 2015, *Sci*, 350, 64
- Madhusudhan, N. 2019, *ARA&A*, 57, 617
- Madhusudhan, N., Sarkar, S., Constantinou, S., et al. 2023, *ApJL*, 956, L13
- Madurowicz, A., Mukherjee, S., Batalha, N., et al. 2023, *AJ*, 165, 238
- Manjavacas, E., Apai, D., Lew, B. W. P., et al. 2019, *ApJL*, 875, L15
- Mansfield, M., Bean, J. L., Line, M. R., et al. 2018, *AJ*, 156, 10
- Mansfield, M., Line, M. R., Bean, J. L., et al. 2021, *NatAst*, 5, 1224
- Marley, M. 2000, in *ASP Conf. Ser.* 212, *From Giant Planets to Cool Stars*, ed. C. A. Griffith & M. S. Marley (San Francisco, CA: ASP), 152
- Marley, M. S., & Robinson, T. D. 2015, *ARA&A*, 53, 279
- Marley, M. S., Saumon, D., & Goldblatt, C. 2010, *ApJL*, 723, L117
- Marley, M. S., Saumon, D., Morley, C., et al. 2021a, *Sonora Bobcat: Cloud-free, Substellar Atmosphere Models, Spectra, Photometry, Evolution, and Chemistry*, Sonora Bobcat, v1, Zenodo, doi:10.5281/zenodo.5063476
- Marley, M. S., Saumon, D., Visscher, C., et al. 2021b, *ApJ*, 920, 85
- Marocco, F., Eisenhardt, P. R. M., Fowler, J. W., et al. 2021, *ApJS*, 253, 8
- Marocco, F., Kirkpatrick, J. D., Schneider, A. C., et al. 2024, *ApJ*, 967, 147
- Matthews, E. C., Carter, A. L., Pathak, P., et al. 2024, *Natur*, 633, 789
- Meisner, A. M., Leggett, S. K., Logsdon, S. E., et al. 2023, *ApJ*, 166, 57
- Mesa, D., Gratton, R., Kervella, P., et al. 2023, *A&A*, 672, A93
- Miles, B. E., Skemer, A. J. I., Morley, C. V., et al. 2020, *AJ*, 160, 63
- Miles, B. E., Biller, B. A., Patapis, P., et al. 2023, *ApJL*, 946, L6
- Miller, N., & Fortney, J. J. 2011, *ApJL*, 736, L29
- Mollière, P., van Boekel, R., Bouwman, J., et al. 2017, *A&A*, 600, A10

- Mollière, P., Stolk, T., Lacour, S., et al. 2020, *A&A*, **640**, A131
- Moran, S. E., Stevenson, K. B., Sing, D. K., et al. 2023, *ApJL*, **948**, L11
- Morley, C. V., Fortney, J. J., Marley, M. S., et al. 2012, *ApJ*, **756**, 172
- Morley, C. V., Marley, M. S., Fortney, J. J., et al. 2014, *ApJ*, **787**, 78
- Morley, C. V., Skemer, A. J., Allers, K. N., et al. 2018, *ApJ*, **858**, 97
- Mukherjee, S., Batalha, N. E., Fortney, J. J., & Marley, M. S. 2023, *ApJ*, **942**, 71
- Mukherjee, S., Fortney, J. J., Batalha, N. E., et al. 2022, *ApJ*, **938**, 107
- Mukherjee, S., Fortney, J. J., Morley, C., et al. 2023a, The Sonora Substellar Atmosphere Models. IV. Elf Owl: Atmospheric Mixing and Chemical Disequilibrium with Varying Metallicity and C/O Ratios (Y-type Models), v1.0, Zenodo, doi:[10.5281/zenodo.10381250](https://doi.org/10.5281/zenodo.10381250)
- Mukherjee, S., Fortney, J. J., Morley, C., et al. 2023b, The Sonora Substellar Atmosphere Models. IV. Elf Owl: Atmospheric Mixing and Chemical Disequilibrium with Varying Metallicity and C/O Ratios (T-type Models), v1, Zenodo, doi:[10.5281/zenodo.10385821](https://doi.org/10.5281/zenodo.10385821)
- Mukherjee, S., Fortney, J. J., Morley, C., et al. 2023c, The Sonora Substellar Atmosphere Models. IV. Elf Owl: Atmospheric Mixing and Chemical Disequilibrium with Varying Metallicity and C/O Ratios (L-type Models), v1, Zenodo, doi:[10.5281/zenodo.10385987](https://doi.org/10.5281/zenodo.10385987)
- Mukherjee, S., Fortney, J. J., Morley, C. V., et al. 2024, *ApJ*, **963**, 73
- NASA Exoplanet Science Institute 2024, Planetary Systems Table, Last retrieved: 2024 June 21, IPAC, doi:[10.26133/NEA12](https://doi.org/10.26133/NEA12)
- Nasedkin, E., Mollière, P., Lacour, S., et al. 2024, *A&A*, **687**, A298
- O'Donoghue, J., Moore, L., Stallard, T. S., & Melin, H. 2016, *Natur*, **536**, 190
- Pérez, F., & Granger, B. E. 2007, *CSE*, **9**, 21
- Petrus, S., Chauvin, G., Bonnefoy, M., et al. 2023, *A&A*, **670**, L9
- Petrus, S., Whiteford, N., Patapis, P., et al. 2024, *ApJL*, **966**, L11
- Phillips, M. W., Liu, M. C., & Zhang, Z. 2024, *ApJ*, **961**, 210
- Phillips, M. W., Tremblin, P., Baraffe, I., et al. 2020, *A&A*, **637**, A38
- Prinn, R. G., & Barshay, S. S. 1977, *Sci*, **198**, 1031
- Radigan, J., Lafrenière, D., Jayawardhana, R., & Artigau, E. 2014, *ApJ*, **793**, 75
- Rice, E. L., Barman, T., McLean, I. S., Prato, L., & Kirkpatrick, J. D. 2010, *ApJS*, **186**, 63
- Rustamkulov, Z., Sing, D. K., Mukherjee, S., et al. 2023, *Natur*, **614**, 659
- Samlund, M., Mollière, P., Bonnefoy, M., et al. 2017, *A&A*, **603**, A57
- Sanghi, A., Liu, M. C., Best, W. M. J., et al. 2023, *ApJ*, **959**, 63
- Saumon, D., Geballe, T. R., Leggett, S. K., et al. 2000, *ApJ*, **541**, 374
- Saumon, D., Hubbard, W. B., Burrows, A., et al. 1996, *ApJ*, **460**, 993
- Saumon, D., Marley, M. S., Abel, M., Frommhold, L., & Freedman, R. S. 2012, *ApJ*, **750**, 74
- Saumon, D., Marley, M. S., Cushing, M. C., et al. 2006, *ApJ*, **647**, 552
- Schneider, A. C., Munn, J. A., Vrba, F. J., et al. 2023, *AJ*, **166**, 103
- Schneider, A. C., Cushing, M. C., Kirkpatrick, J. D., et al. 2015, *ApJ*, **804**, 92
- Schneider, A. D., & Bitsch, B. 2021, *A&A*, **654**, A72
- Schwarz, G. 1978, *AnSta*, **6**, 461
- Showman, A. P., Fortney, J. J., Lian, Y., et al. 2009, *ApJ*, **699**, 564
- Showman, A. P., & Kaspi, Y. 2013, *ApJ*, **776**, 85
- Showman, A. P., Tan, X., & Parmentier, V. 2020, *SSRv*, **216**, 139
- Showman, A. P., Tan, X., & Zhang, X. 2019, *ApJ*, **883**, 4
- Simcoe, R. A., Burgasser, A. J., Bernstein, R. A., et al. 2008, *Proc. SPIE*, **7014**, 70140U
- Sing, D. K., Fortney, J. J., Nikolov, N., et al. 2016, *Natur*, **529**, 59
- Sorahana, S., Suzuki, T. K., & Yamamura, I. 2014, *MNRAS*, **440**, 3675
- Stephens, D. C., Leggett, S. K., Cushing, M. C., et al. 2009, *ApJ*, **702**, 154
- Tan, X., & Showman, A. P. 2019, *ApJ*, **874**, 111
- Tan, X., & Showman, A. P. 2021, *MNRAS*, **502**, 2198
- Tang, S.-Y., Robinson, T. D., Marley, M. S., et al. 2021, *ApJ*, **922**, 26
- Thorngren, D., & Fortney, J. J. 2019, *ApJL*, **874**, L31
- Tokunaga, A. T., Simons, D. A., & Vacca, W. D. 2002, *PASP*, **114**, 180
- Traub, W. A., & Oppenheimer, B. R. 2010, in Exoplanets, ed. S. Seager (Tucson, AZ: Univ. Arizona Press), 111
- Tremblin, P., Amundsen, D. S., Mourier, P., et al. 2015, *ApJL*, **804**, L17
- Tremblin, P., Phillips, M. W., Emery, A., et al. 2020, *A&A*, **643**, A23
- Tremblin, P., Padoleau, T., Phillips, M. W., et al. 2019, *ApJ*, **876**, 144
- Tsai, S.-M., Lee, E. K. H., Powell, D., et al. 2023, *Natur*, **617**, 483
- Virtanen, P., Gommers, R., Oliphant, T. E., et al. 2020, *NatMe*, **17**, 261
- Vorobyov, E. I. 2013, *A&A*, **552**, A129
- Vos, J. M., Faherty, J. K., Gagné, J., et al. 2022, *ApJ*, **924**, 68
- Wang, J. J., Ruffio, J.-B., Morris, E., et al. 2021, *AJ*, **162**, 148
- Welbanks, L., Madhusudhan, N., Allard, N. F., et al. 2019, *ApJL*, **887**, L20
- Wordsworth, R., & Kreidberg, L. 2022, *ARA&A*, **60**, 159
- Xuan, J. W., Wang, J., Finnerty, L., et al. 2024a, *ApJ*, **962**, 10
- Xuan, J. W., Hsu, C.-C., Finnerty, L., et al. 2024b, *ApJ*, **970**, 71
- Zahnle, K. J., & Marley, M. S. 2014, *ApJ*, **797**, 41
- Zalesky, J. A., Line, M. R., Schneider, A. C., & Patience, J. 2019, *ApJ*, **877**, 24
- Zalesky, J. A., Saboi, K., Line, M. R., et al. 2022, *ApJ*, **936**, 44
- Zhang, X. 2020, *RAA*, **20**, 099
- Zhang, X., & Showman, A. P. 2014, *ApJL*, **788**, L6
- Zhang, Y., Snellen, I. A. G., Bohn, A. J., et al. 2021, *Natur*, **595**, 370
- Zhang, Z. 2024a, *RNAAS*, **8**, 114
- Zhang, Z., Liu, M. C., Clayton, Z. R., et al. 2021a, *ApJL*, **916**, L11
- Zhang, Z., Liu, M. C., Marley, M. S., Line, M. R., & Best, W. M. J. 2021b, *ApJ*, **916**, 53
- Zhang, Z., Liu, M. C., Marley, M. S., Line, M. R., & Best, W. M. J. 2021c, *ApJ*, **921**, 95
- Zhang, Z., Liu, M. C., Hermes, J. J., et al. 2020, *ApJ*, **891**, 171
- Zhang, Z., Mollière, P., Hawkins, K., et al. 2023a, *AJ*, **166**, 198
- Zhang, Z., Marley, C. V., Gully-Santiago, M., et al. 2023b, *SciA*, **9**, eadbf8736
- Zhang, Z., Mukherjee, S., Liu, M., et al. 2024b, Disequilibrium Chemistry, Diabatic Thermal Structure, and Clouds in the Atmosphere of COCONUTS-2b, v1, Zenodo, doi:[10.5281/zenodo.13975825](https://doi.org/10.5281/zenodo.13975825)
- Zhou, Y., Apai, D., Schneider, G. H., Marley, M. S., & Showman, A. P. 2016, *ApJ*, **818**, 176
- Zhou, Y., Bowler, B. P., Apai, D., et al. 2022, *AJ*, **164**, 239
- Zieba, S., Kreidberg, L., Ducrot, E., et al. 2023, *Natur*, **620**, 746
- Zuckerman, B., & Song, I. 2009, *A&A*, **493**, 1149